Crystal Barrel Internal Note 316

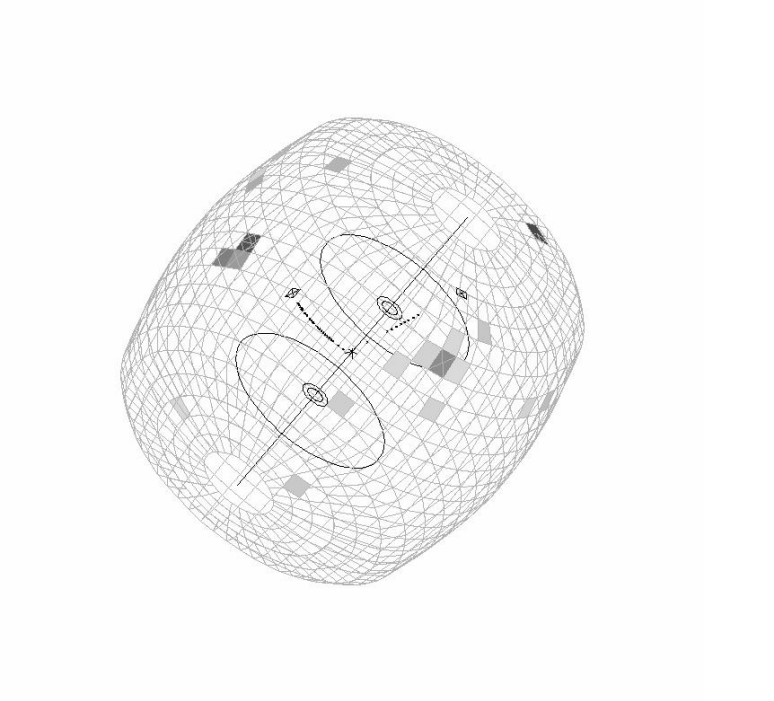

Technical Report: Analysis of $\eta\eta\pi^0$ at 1.94 GeV/c

Jörg Lüdemann

DESY, Hamburg

Holger Stöck

Ruhr-Universität Bochum

Titlepage Picture: Event Display PERNOD written by Rüdiger Berlich / MPI, Munich

Abstract

Antiproton-proton annihilation into $\pi^0\eta\eta$ with incident antiproton beam momentum of 1940 MeV/c has been studied. The data were taken with a trigger on antiproton interaction, zero charged tracks and calorimeter energy sum in order to aquire only all neutral final states. The conclusions reached by this work are based mainly on 6γ-data, but are backed up by the analysis of the $\pi^0\eta\eta$-channel in the 10γ decay mode.
To fit the data a partial wave analysis using the canonical description of the particle states was performed. It turned out that four already known resonances were needed: $a_0(980)$, $a_2(1320)$, $f_2(1270)$, $f_0(1500)$. In addition two new resonances, a $f_J(2100)$ and an $a_2(1680)$, were necessary for a reasonable description.

Contents

Chapter 1

Reconstruction and selection

The data taken at incident antiproton beam momentum of 1.94 GeV/c were recorded in July 1992 and August 1994. Almost all data were taken with a zero-prong trigger requiring a reacting antiproton in the target defined by the entrance counters and no signal from the veto counters downstream behind the target. Furthermore neither hits in the PWCs nor in the inner most three layers of the JDC were demanded. Additionally, a lower threshold in the fast FERA energy sum (Tony's box) was set.

For the studied reactions only π^0's and η's decaying into two photons were considered. The final states $3\pi^0$, $2\pi^0\eta$, $\pi^0\eta\eta$ and 3η were reconstructed from six measured photon hits in the electromagnetic calorimeter.

Although only the final state $\pi^0\eta\eta$ is discussed in this technical report the reconstruction and selection procedure is reported for all other final states for referencing in further technical reports. For the reconstruction standard CB software was applied to the data: CBOFF 1.27/05, LOCATER 1.97/04, BCTRAK 2.03/00, GTRACK 1.34/01. These libraries were interfaced with CBoOff++.

1.1 Reconstruction of the photons

The photon reconstruction procedure was very similar to the one used on data at rest. A special treatment was not necessary, unlike for the data on two body annihilations. The standard cut of 1 MeV as minimum energy deposit per crystal was applied for photon reconstruction. Clusters and PEDs with energy deposits less than 20 MeV were rejected. The energies were corrected using the updated energy correction function [6]. In order to obtain an improved spatial resolution the "Rainer Glantz" PED smoothing (PDRG flag set in BCTRAK) was applied [4]. The reconstructed values for θ are corrected by about 10 mrad for PEDs with central crystal type 11-13.

All Monte Carlo studies were done using CBGEANT 4.06/07 based on GEANT 3.15/90. Efficiencies and acceptances were estimated with the help of Monte Carlo simulations.

1.2 Preselection

The cuts of the preselection are:

- **no charged track** from LOCATER
- **exactly six photons** from BCTRAK. Only Peds with energy deposits greater than 20 MeV are considered.

Spectrum (a) in figure 1.1 shows the multiplicity of charged tracks for the all neutral triggered data. The multiplicity of photons after rejection of charged events is shown in spectrum (b).

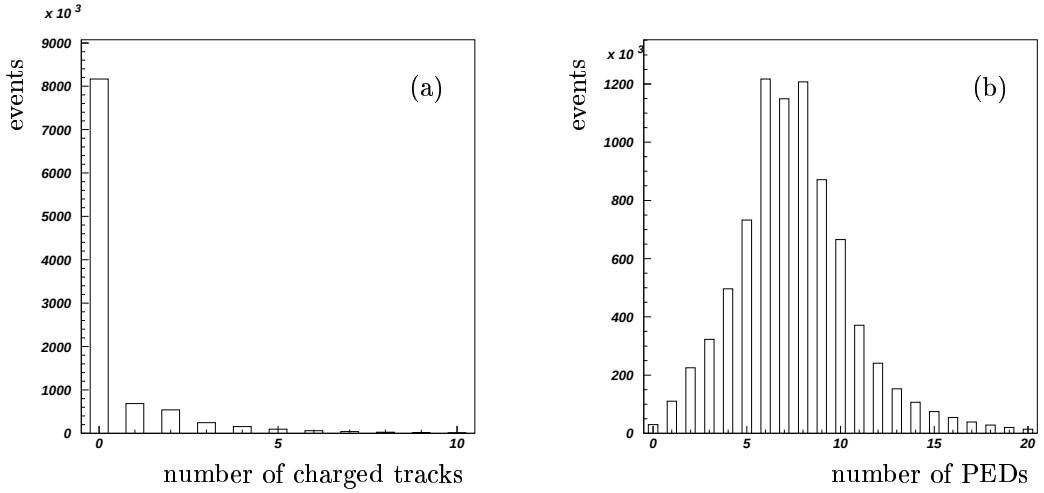

Figure 1.1: **Multiplicities before preselection.** *Spectrum (a) shows the multiplicity of charged tracks. In spectrum (b) the multiplicity of PEDs after rejection of charged events is shown.*

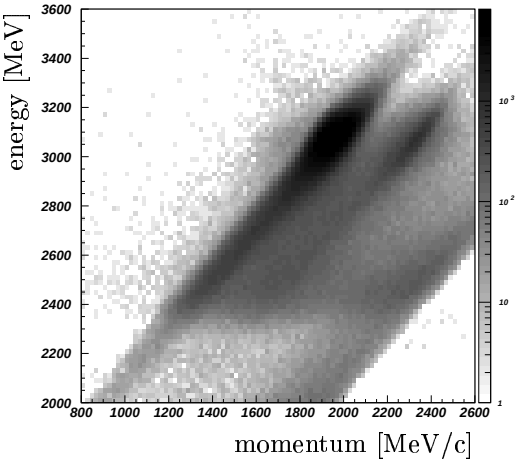

Figure 1.2: **Total energy versus total momentum.** *The number of entries in each cell is drawn on a logarithmic scale to emphasize weak structures. Besides the strong enhancement where fully reconstructed events are expected (momentum=1940 MeV/c, energy = 3093 MeV) regions can be identified where one photon was missing (diagonal band). The reoccurence of a similar structure at higher momenta is resulting from reactions in the veto counter, which were not completely excluded. These events were recorded but the photon momenta were not calculated correctly.*

A preselection cut on total energy and momentum was not applied. Complete events are more effectively recognized and selected by means of a constraint kinematical fit. In figure

1.2 the distribution of total energy versus total momentum of pure neutral events is shown. Due to the hermiticity of the detector and the required minimum energy deposited in the calorimeter most of the events fulfill already the energy momentum balance within the experimental errors. Cuts typically applied in analyses of data at rest were carefully studied. However, the rejection of events with PEDs in the outermost crystals (crystal type 13) is fatal when analyzing reactions in flight. Due to the expected leakage losses at the edge of the calorimeter this cut is reasonable, but it reduces the covered solid angle in the center of mass system drastically for data in flight. Actually a large fraction of those events are of high quality and badly measured events are rejected later on by the constraint fit. Similary a cut vetoing events as pile-up-events was not applied. Real pile-up-events are rejected by the further selection and many good events were flagged as pile-up. Also no split-off recognition algorithm was applied to the data, as the background of five photon events with one additional electromagnetic split-off could be well estimated and suppressed more efficiently by other means.

1.3 Constraint fit

The complete measurement of all particles in the final state and the determination of their kinematics allows a constraint fit to improve the data quality. Moreover such a constraint fit yields the possibility to test hypotheses, so that events can be classified. Another output of an successfully converged fit are four-vectors which fulfill the imposed constraints. As this method is not implemented correctly for purely neutral final states in flight into CBKFIT, a selfmade code was used. This code fits all measured kinematical quantities of six photons (θ, φ, $\sqrt{E}$) and allows for a freely adjustable z-coordinate of the primary reaction vertex. The formulas involved can be found in [1]. CBKFIT (CASE.EQ.6) has not been used because there the vertex's position is calculated by newton iteration from the photon z-momenta and then treated in the fit as measured quantity with a fixed error. This treatment gives rise to large covariances among most of the involved quantities which is not taken into account in CBKFIT, where all off-diagonal elements of the covariance matrix are fixed to zero and also an evaluation of the true error of measurement of the vertex position by means of error propagation is not implemented. It turns out that the actually used method in this analysis is not only the correct mathematical formulation but also improves the selection and reconstruction chain with respect to efficiency, invariant mass resolution and separation of final states by confidence levels.

Kinematical fits were applied testing the following hypotheses:

(1) $\overline{p}p \longrightarrow 6\gamma$

(2) $\overline{p}p \longrightarrow \pi^0\pi^0\gamma\gamma$

(3) $\overline{p}p \longrightarrow \pi^0\pi^0\pi^0$

(4) $\overline{p}p \longrightarrow \pi^0\pi^0\eta$

(5) $\overline{p}p \longrightarrow \pi^0\eta\eta$

(6) $\overline{p}p \longrightarrow \eta\eta\eta$

For the hypotheses 2, 4 and 5 45 permutations of the sequence of six photons and for hypotheses 3 and 6 15 permutations were tried. In order to minimize CPU time the permutations of interest are preselected by windows in the invariant mass. The boundaries

of these were chosen large enough not to lose any event: 70-200 MeV/c^2 for pions and 450-650 MeV/c^2 for η mesons.

1.3.1 Errors of the measured quantities

The prerequisite for the application of a constraint fit is the knowledge of the errors of measurement. The error in $\sqrt{E}$ is estimated to

$$\sigma(\sqrt{E})/E = 2.8\%/\sqrt{E}\ , \quad E\ in\ GeV \tag{1.1}$$

A lower limit of $\sigma(\sqrt{E}) > 0.35$ MeV$^{1/2}$ is superimposed. The errors σ for φ and θ were determined in [4] for energies up to 1 GeV for crystal types 1 to 12 and parametrized by

$$\sigma = p_1 + p_2\sqrt{E} + p_3\ ln(E)\ , \quad E\ in\ MeV \tag{1.2}$$

The parameters p_1, p_2 and p_3 were determined separately for the cases of one or several PEDs per cluster and separately for edge and central crystals. A Monte Carlo study showed that this parametrisation cannot be used for photon energies higher than 1 GeV which frequently occur in in flight reactions. Therefore the errors as calculated by BCTRAK were not used for φ and θ. They were overwritten by values based on a study of the reconstruction of Monte Carlo events generated with 1.94 GeV/c antiproton momentum (Tab. 1.1). These new estimates had to be scaled for the kinematical fit (Tab. 1.2) in order to compensate for systematical difficulties, e.g. the non-gaussian distribution of the error of energies. These scaling factors had to be determined separately for data measured under different conditions and for Monte Carlo events by adjusting the widths of the pull distributions resulting from the constraint fit. The good estimate of the errors shows up in a flat distribution of the confidence level for events which are fitted with the correct hypothesis (fig. 1.3).

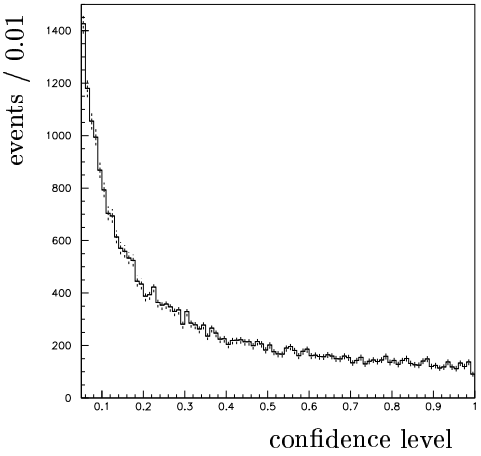

Figure 1.3: **Confidence level distribution for the hypothesis $\overline{p}p \to \pi^0\eta\eta$ at 1940 MeV/c.** *The distribution should be flat for events which fulfill the hypothesis. The rise at low values originates from events of other misidentified reactions, where the fit yields a low confidence level.*

	PEDs / Cluster	Type		σ in mrad (E in GeV)	E_0 in GeV
φ	1	1 - 10		27.26 - 35.68 E + 30.38 E^2 - 9.28 E^3	1.4
		11 - 13		53.89 - 65.15 E + 48.15 E^2 - 12.8 E^3	1.6
	2	1 - 10	hi	24.36 - 23.92 E + 17.79 E^2 - 4.99 E^3	1.5
			lo	= hi / 0.93	
		11 - 13	hi	47.98 - 48.3 E + 35.85 E^2 - 9.76 E^3	1.8
			lo	= hi / 0.88	
θ	1	1 - 10		27.3 - 49.69 E + 67.16 E^2 - 43 E^3 + 10 E^4	1.5
		11		10 + 7(1 - E/1.5)	1.5
		12		10 + 13(1 - E/1.5)	
		13		9 + 6(1 - E/1.5)	
	2	1 - 10	hi	25 - 39.67 E + 58.28 E^2 - 41.18 E^3 + 10.32 E^4	1.5
			lo	= hi / 0.91	
		11 - 13		23 - 32.26 E + 23.16 E^2 - 30.16 E^3 + 11.32 E^4	1.4

Table 1.1: **Estimation of errors for φ and θ.** *The errors depend on the number of PEDs per cluster and the type of the central crystal of the PED. In most cases with 2 (or more) PEDs per cluster it has to be distincted, whether the PED has the largest energy deposit in the cluster (hi) or not (lo). E_0 is the photon energy up to which the error was parametrized. For higher energies the error at $E = E_0$ is used.*

	σ^2_φ	σ^2_θ	$\sigma^2_{\sqrt{E}}$
Monte Carlo	1.57	1.20	1.02
July 1992	1.18	1.00	0.97
August 1994	1.40	1.10	1.00

Table 1.2: **Scaling factors for the errors.** *These factors scale the squared errors in order to compensate differences in the data samples and inadequacies of the Monte Carlo simulation.*

1.4 Selection of the 6γ final state

After the kinematical fit with a free z-vertex events were rejected if none of the final state hypotheses ($3\pi^0$, $2\pi^0\eta$, $\pi^0\eta\eta$, 3η) converged with a confidence level of at least 10% or the fitted z-coordinate of the vertex was outside the target volume (-5 cm < z < 5 cm). The events were classified to originate from a certain kind of reaction according to the hypothesis yielding the highest confidence level. Finally a suppression of 'cross talk' between the final states was applied using the criteria listed in table 1.3.

	confidence level of constraint fit			
classified	3 π^0	2 $\pi^0\eta$	$\pi^0\eta\eta$	3 η
3 π^0	> 10 %	$<$**10^{-3}**	-	-
2 $\pi^0\eta$	$< 10^{-5}$	> 10 %	-	-
$\pi^0\eta\eta$	$< 10^{-5}$	$< 10^{-5}$	> 10 %	< 10 %
3 η	$< 10^{-5}$	$< 10^{-5}$	$< 10^{-5}$	> 10 %

Table 1.3: **Separation and classification of final states.** *The table shows upper and lower limits for the confidence levels of the tested hypothesis. Emphasized: the restrictive veto cut for the final state 3 π^0 against events of the type $2\pi^0\eta$, which accounts for a visible structure in the acceptance Dalitz plot for the 3 π^0-channel (fig. 1.4).*

With the help of Monte Carlo events undergoing the same chain of reconstruction and selection as real data efficiencies could be estimated. The values for efficiencies and rates for false classification are given in table 1.4. They result as the ratio of the number of classified events of a certain reaction type and the number of generated Monte Carlo events. The final states $\pi^0\omega$ and $\eta\omega$, with $\omega \to \pi^0\gamma$, are considered to be the most prominent sources of background [2]. In these cases an electromagnetic split-off is misidentified as a photon. As this background can be suppressed sufficiently by the kinematic fitting procedure (Tab. 1.4) no further treatment of split-offs was applied.

	generated final state (Monte Carlo)							
classified	3 π^0	2 $\pi^0\eta$	$\pi^0\eta\eta$	3 η	$\pi^0\omega$	$\eta\omega$	$\omega\omega$	$4\pi^0$
3 π^0	**26.6 %**	$6{\cdot}10^{-5}$	$2{\cdot}10^{-4}$	$3{\cdot}10^{-5}$	$4{\cdot}10^{-3}$	$3{\cdot}10^{-5}$	$5{\cdot}10^{-3}$	$5{\cdot}10^{-4}$
2 $\pi^0\eta$	$6{\cdot}10^{-4}$	**29.5 %**	$1{\cdot}10^{-3}$	$6{\cdot}10^{-4}$	$1{\cdot}10^{-3}$	$4{\cdot}10^{-3}$	$2{\cdot}10^{-2}$	$1{\cdot}10^{-3}$
$\pi^0\eta\eta$	$3{\cdot}10^{-5}$	$4{\cdot}10^{-5}$	**23.5 %**	$1{\cdot}10^{-3}$	$3{\cdot}10^{-5}$	$6{\cdot}10^{-4}$	$3{\cdot}10^{-4}$	0
3 η	0	$1{\cdot}10^{-5}$	$1{\cdot}10^{-4}$	**25.2 %**	0	$3{\cdot}10^{-5}$	$1{\cdot}10^{-5}$	0

Table 1.4: **Efficiencies and 'cross talk'.** *For each final state with three pseudoscalar mesons approximately 100.000 events were simulated and reconstructed, 50.000 for the $4\pi^0$ channel, about 30.000 for each of the background channels with one omega meson and 100.000 for the $\omega\omega$ final state. Each Monte Carlo channel was generated only for the 6γ final state.*

Neither in the Dalitz plots nor in the spectra of production angles structures are visible in the acceptance (fig. 1.4). The acceptance is almost flat and goes down for production angles close to the beam axis $|cos\Theta| = 1$. However, in the final state 3 π^0 at $\pi^0\pi^0$-invariant masses close to the $\pi^0\eta$ threshold, $m^2 \sim 0.47$ GeV^2/c^4, a lack of acceptance is visible in the Dalitz plot. This is due to the restrictive veto cut against events of the type $\overline{p}p \to \pi^0\pi^0\eta$ (Tab. 1.3) which rejects also events of the type $\overline{p}p \to 3\pi^0$.

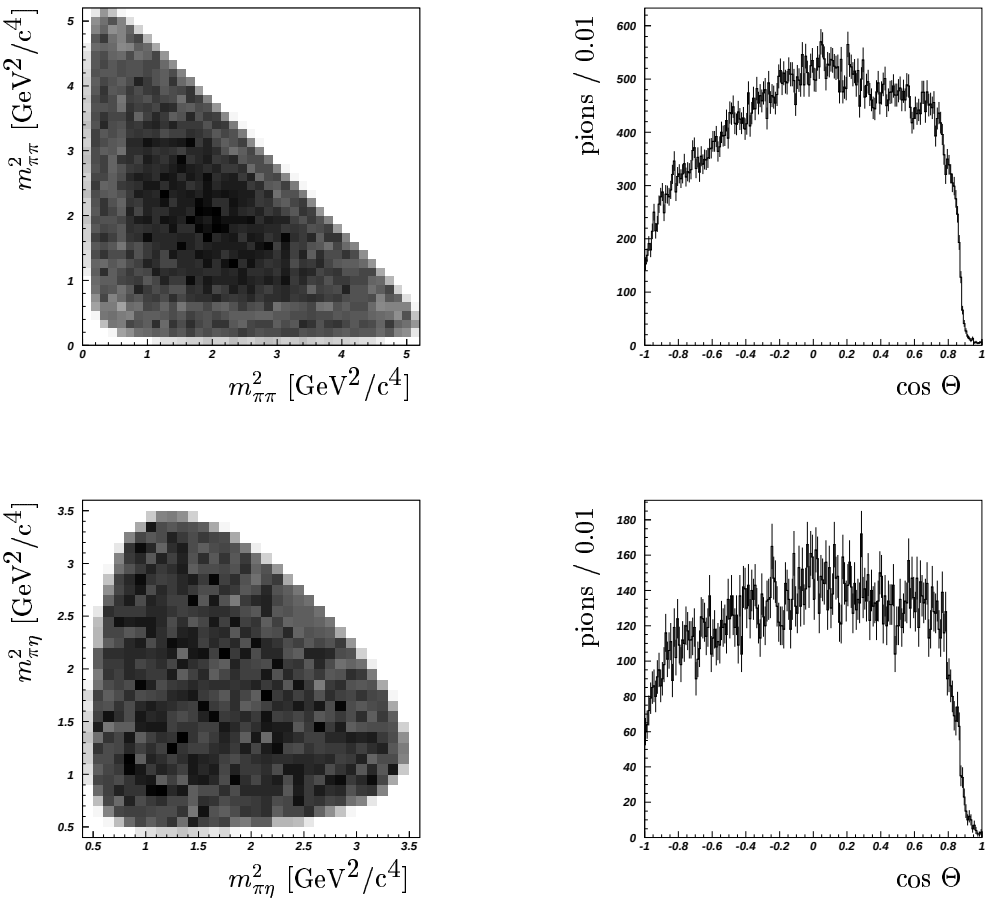

Figure 1.4: **Acceptances for final states $3\pi^0$ and $\pi^0\eta\eta$.** *On the left hand side are shown Dalitz plots for Monte Carlo generated events. In the final state $3\pi^0$ a lack of acceptance originates from a rigorous cut against the final state $\pi^0\pi^0\eta$ at $\pi^0\pi^0$-masses close to the $\pi^0\eta$-threshold. On the right hand side are shown the distributions of the cosine of the production angle which are defined as the angle between the direction of flight of a pion and the beam axis measured in the overall center of mass system.*

The selection was applied to 10.5 million events taken with an incident antiproton beam momentum of 1.94 GeV/c resulting in the numbers of events given in table 1.5.

	July 1992	**August 1994**		Σ	
trigger	zero prong	zero prong	mixed (0 or 2 pr.)		
physics events	6327591	3273663	440776		
no charged tracks	5236469	2492941	436816		
6 PEDs	824013	317960	74823		
one hyp. > 0.1	171752	103133	25918		
$\pi^0\pi^0\pi^0$	108211	67773	17099	197016	(193083)
$\pi^0\pi^0\eta$	52174	32904	8236	95285	(93314)
$\pi^0\eta\eta$	3220	2032	467	5830	(5719)
$\eta\eta\eta$	241	171	47	472	(459)

Table 1.5: **Results from the selection.** *The table shows the number of events surviving the individual steps of the selection chain for the three different data samples. The sample 'mixed trigger' was already roughly preselected with a veto against charged tracks. As the selection history for a fraction of the sample from July 92 is not available due to technical problems the actual number of selected events is slightly larger than the one given in column 2. The right most column show the total number of really reconstructed events (the sum of the left columns is given in brackets).*

The quality of the data is best shown in $\gamma\gamma$-invariant mass plots. The spectrum of the $\gamma\gamma$ invariant mass for events passing a constraint fit to the hypothesis $\overline{p}p \to 6\gamma$ with a confidence level better than 1% ist plotted in figure 1.5 (a). The signals of π^0 and η are clearly visible above the combinatorical background (15 entries per event). The signals from the η' decaying to $\gamma\gamma$ and from the ω decaying to $\pi^0\gamma$, where one low-energetic photon from the π^0 decay is not detected, are shown in figure 1.5 (b). In this plot the $\gamma\gamma$ invariant mass is shown from the converged (confidence level > 10%) hypothesis $\overline{p}p \to \pi^0\pi^0\gamma\gamma$, where events fulfilling the hypothesis $\overline{p}p \to 3\pi^0$ (confidence level > 10^{-5}) were disregarded. In the mass region 620 to 1000 MeV/c^2 this spectrum can be described by the sum of two gaussians and a linear term. The gaussian width of the high mass peak (η') gives an estimate for the resolution at high masses: σ=20.2 MeV/c^2. Fig. 1.6 shows the $\gamma\gamma$ invariant mass near the η-mass, where the mass resolution is $\sigma = 14.6$ MeV/c^2.

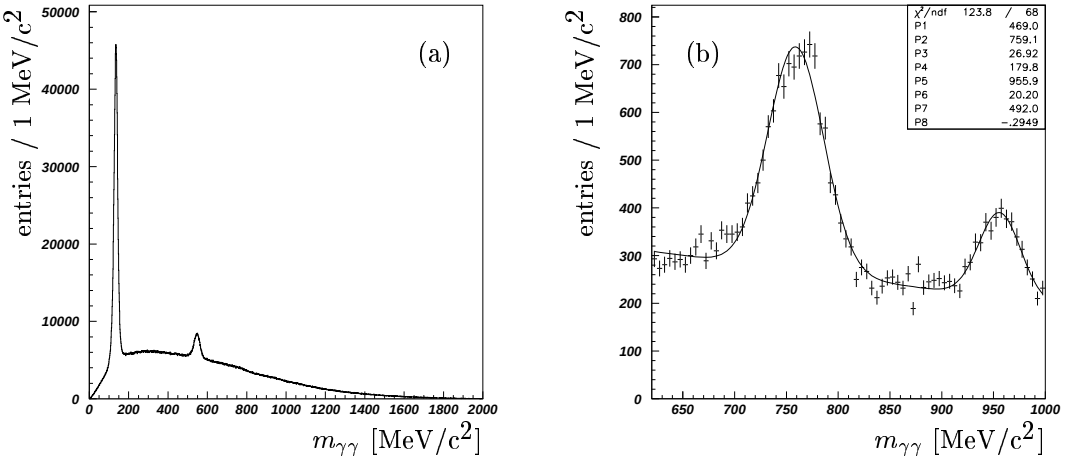

Figure 1.5: $\gamma\gamma$ **invariant mass.** *Spectrum (a): Above the combinatorical background appear the signals from the π^0 and the η-meson. Spectrum (b): $\gamma\gamma$ invariant mass from the channel $\overline{p}p \to \pi^0\pi^0\gamma\gamma$. Signals from ω and η' are visible in the region 620 - 1000 MeV/c^2. A fit of the sum of two gaussians and a linear term yields σ=20.2 MeV/c^2 for the η' peak at 958 MeV/c^2.*

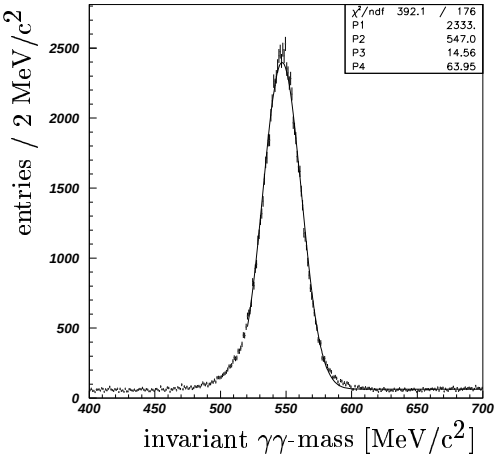

Figure 1.6: **Resolution of the $\gamma\gamma$-invariant mass.** *Data with c.l. > 10 % for the $2\pi^0\gamma\gamma$-hypothesis (c.l. > 10%) and c.l. < 10^{-5} for the $3\pi^0$-hypothesis. The resolution near the η-mass is σ=14.6 MeV/c^2.*

1.5 Presentation of the $\pi^0\eta\eta$ data

The Dalitz plot and the spectra of the invariant masses of the reaction $\overline{p}p \to \pi^0\eta\eta$ are shown in figure 1.7. Besides the signals from the isovectors $a_0(980)$ and $a_2(1320)$ and a clearly visible band at $\eta\eta$ invariant masses around 1500 MeV/c^2 there are hints for

structures at high $\eta\eta$ masses (2100 MeV/c^2) in the lower left corner of the Dalitz plots strongly hidden by the crossing of the $a_0(980)$ bands. Moreover there is an almost invisible structure at low $\eta\eta$ masses possibly originating from the interfering isovectorial amplitudes. The Dalitz plot is also given in a non-symmetric representation. The strong enhancement at high $\eta\eta$ masses seems not to be due to the a_0 only.

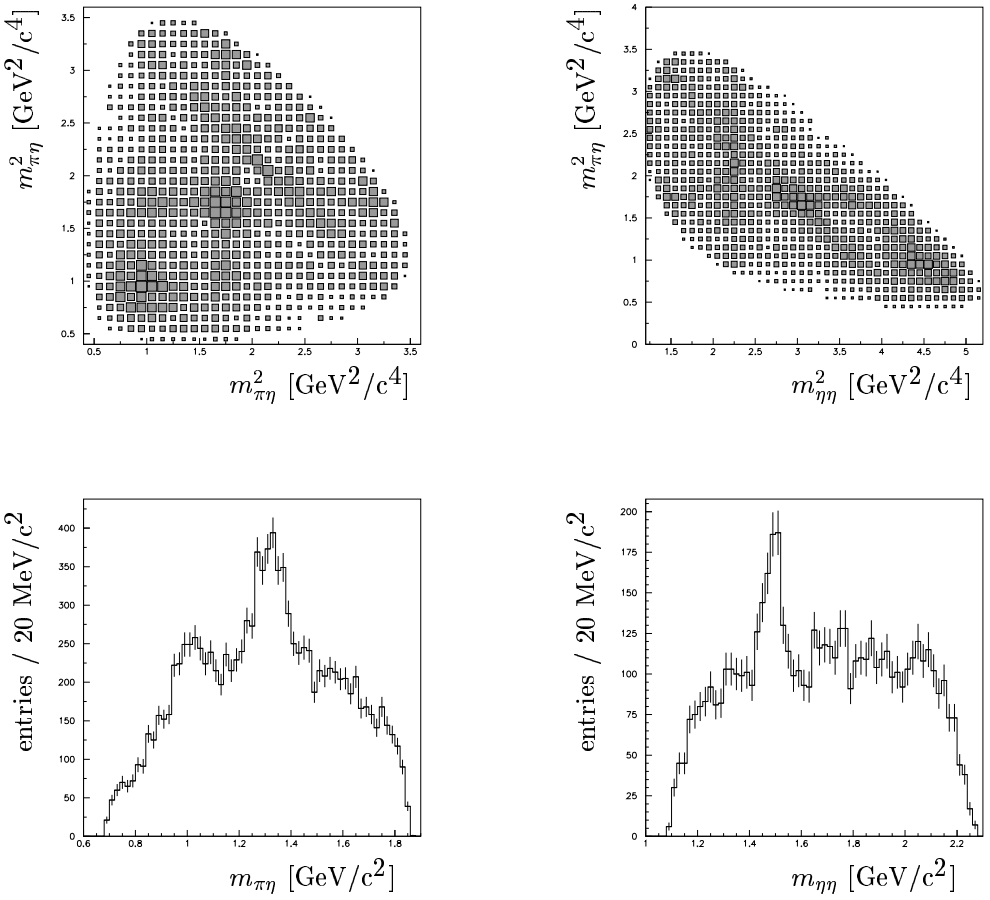

Figure 1.7: **Dalitz plot and invariant mass spectra of the final state $\pi^0\eta\eta$.**

Chapter 2

Partial wave analysis

The advantage of a complete analysis using helicity amplitudes is that it yields information about the contributing initial states. Furthermore it describes the contribution of measured events in all four dimensions of phase space.
As many higher spin initial states contribute to $\overline{p}p$ reactions at 1940 MeV/c [2], a simplified ansatz has to be applied to fit the final state $\overline{p}p \to \pi^0\eta\eta$. This model has already been used to describe the reaction $\overline{p}p \to \pi^0\pi^0\pi^0\eta$ at 1200 and 1940 MeV/c [3].

2.1 Canonical description of the particle states

For a detailed description see CB-note 273 [3]. Here we give only a short review. In the canonical formulation the z-axes of all systems are oriented parallel to each other. We discuss the reaction $\overline{p}p \to$ A+B, where B carries no spin, and the spherical angles of the direction of flight of particle A in the overall center of mass system are (Θ, Φ) with the z-direction parallel to the $\bar{p}$-beam direction. All four-vectors of the final state particles, measured in the overall center of mass system, are then rotated in such way that the direction of flight of particle A is along the z-axis. This is done by a rotation of the coordinate system with Φ around the beam axis and a subsequent rotation with Θ around the new y-axis. After a Lorentz boost anti-parallel to the new z-axis which transforms all four-vectors into the center of mass system of A the whole system is rotated back by $-\Theta$ and $-\Phi$ (Wick rotation). In this canonical system the spherical angles ϑ and φ of the decay of A are defined as the direction of flight of one daughter of A.

The projection λ_i of the total spin J of the $\overline{p}p$ system must be either -1, 0 or 1 because the relative orbital angular momentum is perpendicular to the beam axis. As the $\overline{p}p$-initial state is not polarized, in the differential cross section the interference terms between these three spin substates vanish. With l being the orbital angular momentum between A and B in the overall center of mass system, l_z its projection along the z-axis (beam axis), and λ_f the projection of the spin s of particle A along the z-axis, the coupling between the initial $\bar{p}p$-state and the 2-body state (A+B) is given by

$$|J, \lambda_i\rangle = \sum_{\lambda_f, l_z, l} \langle s\lambda_f l l_z | J\lambda_i\rangle |s, \lambda_f\rangle |l, l_z\rangle. \tag{2.1}$$

The eigenstate of the angular momentum is represented by a Legendre polynomial

$$|l, l_z\rangle = P_l^{l_z}(\Theta, \Phi) \tag{2.2}$$

and the decaying state with spin s by

$$|s, \lambda_f\rangle = P_s^{\lambda_f}(\vartheta, \varphi), \tag{2.3}$$

if both decay products have spin 0.
Due to conservation of the total magnetic spin sub-quantum number M in the process amplitudes belonging to different λ_i add up incoherently.

Also the amplitude for different λ_f add incoherently. This is due to the relation $\lambda_i = \lambda_f + l_z$. The latter statement is correct if all transitions origin from interfering initial states with the same relative phases. The formalism used here, however, integrates over all possible initial $\bar{p}p$-states, thus the summation contains beside the incoherent parts also coherent parts originating from states with different phases. To account for that the amount of interference between two amplitudes of the same λ_f is added as a free parameter. In the case of two interfering amplitudes e.g., instead to just fit the strengths a and b of the two amplitudes and their relative phase φ_{ab} an additional real parameter c_{ab} is introduced which describes the amount of interference, accounting for the presence of more than one contributing initial $\bar{p}p$-state, thus simulating the production process in a crude way. The intensity in a given phase space element τ is given by

$$I(\tau) = a^2|A|^2 + b^2|B|^2 + c_{ab}\ ab(cos\varphi_{ab}\ Re(AB^*) + sin\varphi_{ab}\ Im(AB^*)) \tag{2.4}$$

with the value of c_{ab} limited to the interval -2 to +2.
This formulation appears as being attractive due to the reduced number of free variables in the fit. For each resonance i with spin σ_i there are σ_i+1 real parameters. Additional parameters are introduced to take interferences into account. They describe the relative phases between interfering amplitudes and the strength of interference. This method allows to switch interferences on and off whenever it is clear that they must be included or can be omitted (e.g. if the bands of the resonances do not overlap in the Dalitz plot). For example for a fit of

$$\overline{p}p(0^{-+}, 1^{++}, 2^{++}, 2^{-+}) \longrightarrow \pi^0 + [f_2(1270), f_0(1500), f_2(1640)]$$

there would be 7 free parameters with no interferences. One of the parameters can be fixed by the overall normalization, so that 6 parameters are left. Masses and widths corresponding to 6 further parameters can only be handled as fixed due to the software implementation. They have to be varied 'by hand' or can be scanned. Giving freedom to the fit to adjust all interferences there are 5 additional real parameters for the interfering strengths c_{ab} (there are different parameters allowed for different λ values) and 3 further parameters for relative phases φ_{ab}, one of them being fixed. The number of parameters (in this example 19 including masses and widths) is independent of the assumed initial states in the hypotheses and does only depend on the number of resonances involved.

2.2 Likelihood fit

The fit of the amplitudes to the data was performed using maximum likelihood methods. If p is the probability to observe an event at an elementary phase space volume at point τ, then the probability P to observe a set of events distributed according to a weight function p=w($\tau, \vec{x}$) ($\vec{x}$ the vector of adjustable parameters) is given by the product of all probabilities multiplied by n! (n = number of events) as the order of events does not

matter. The likelihood is defined in the same sense for a weight function representing probability densities with arbitrary normalization:

$$L = n! \prod_{i=1}^{n} \frac{w(\tau_i, \vec{x})\ \epsilon(\tau_i)}{\int w(\tau_i, \vec{x})\ \epsilon(\tau_i)\ d\tau} \tag{2.5}$$

The acceptance of the apparatus and the efficiency of reconstruction are described by ϵ, the free parameters in the weight function by $\vec{x}$. The integral in the denominator extends over the kinematically allowed region of the multi-dimensional phase space. The product runs over all measured events i at phase space point τ_i. The integral is needed to normalize the weight function and prevent it from diverging during the fitting procedure. For technical reasons the quantity to be minimized is taken to be the negative logarithmic likelihood NLL

$$NLL = -logL \tag{2.6}$$

The integral $\Theta = \int w(\tau, \vec{x})\ \epsilon(\tau)\ d\tau$ is approximated numerically via the summation of the weight function over a sample of Monte Carlo events. As these undergo the same influences of acceptance and efficiency as the data the factor ϵ is already considered implicitly. With m the number of Monte Carlo events the approximation reads

$$\Theta = \frac{n}{m} \sum_{j=1}^{m} w(\tau_j^{MC}, \vec{x}) = \frac{n}{m} \Phi \tag{2.7}$$

By neglecting all constant terms (terms not depending on $\vec{x}$) which do not affect the optimization procedure the calculated value of NLL is

$$NLL = -\sum_{i=1}^{n} log(w(\tau_i, \vec{x})) + n\ log\left(\frac{\Phi}{m}\right) \tag{2.8}$$

An improvement of the thus defined NLL of $0.5 \cdot$ r by extending the hypotheses by r more free variables corresponds to a change of one in the reduced χ^2 to r degrees of freedom. Therefore a reduction on NLL of more than 0.5 per added fit parameter has to be considered as significant (one standard deviation). Similary the error of a fitted parameter can be estimated by scanning it in the neighborhood of the found value (all other parameters fixed). Ideally the NLL should behave like a parabola. In a distance of one (two) standard deviation σ the value of NLL increases by 0.5 (2).

For fitting the minimization package FUMILI was chosen.

Chapter 3

Results of the analysis

3.1 Basic fit on a reduced Dalitz plot

To start on a save ground we excluded the $\eta\eta$ high mass region from the first fit. We applied a cut on $m^2(\eta\eta) > 3.8$ GeV^2 and ended up with 4.465 data and 18.836 Monte Carlo events. The reduced Dalitz plots are shown in fig. 3.1.

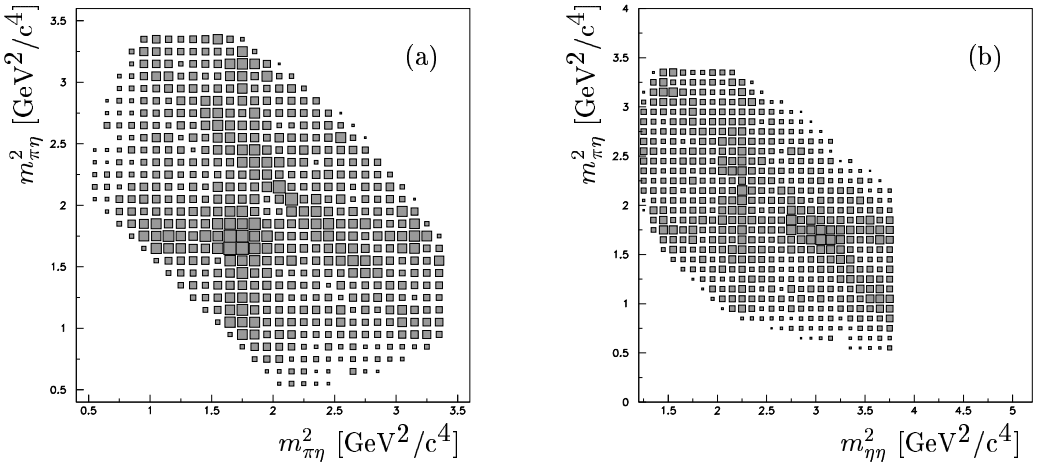

Figure 3.1: **Reduced Dalitz plot $\pi^0\eta\eta$.** *The symmetric (a) and asymmetric (b) Dalitz plots are shown. The bin size is 0.1 GeV^2/c^4.*

Ingredients to the basic fit were the following resonances and interferences.

Resonances	Interferences
$a_0(980)$	$a_0(980) \times a_2(1320)$
$a_2(1320)$	$a_0(980) \times f_0(1500)$
$f_2(1270)$	$a_0(980) \times a_0(980)$
$f_0(1500)$	$a_2(1320) \times f_2(1270)$
	$a_2(1320) \times f_0(1500)$
	$a_2(1320) \times a_2(1320)$

Table 3.1: **Obvious ingredients for a basic fit.** *These structures are clearly visible in the Dalitz plot.*

Selfinterference means the interference between the amplitude evaluated for one $\pi^0\eta$-combination with the same amplitude taken for the other $\pi^0\eta$-pair. We have chosen a Breit-Wigner form to describe the resonances. In table 3.2 the used masses and widths are given.

Resonance	mass [MeV]	width [MeV]
$a_0(980)$	990	140
$a_2(1320)$	1330	190
$f_2(1270)$	1250	230
$f_0(1500)$	1480	70

Table 3.2: **Masses and widths used for the basic fit.** *These values are used in the Breit-Wigner forms of the resonances.*

Dealing with 23 parameters the fit converged to a negative logarithmic likelihood (NLL) of -425. The Dalitz plot and the mass projections are shown in fig. 3.2. The four basic resonances are describing the data in an almost satisfaying way. In the next steps new resonances are introduced in turn to test whether their contribution is significant or not.

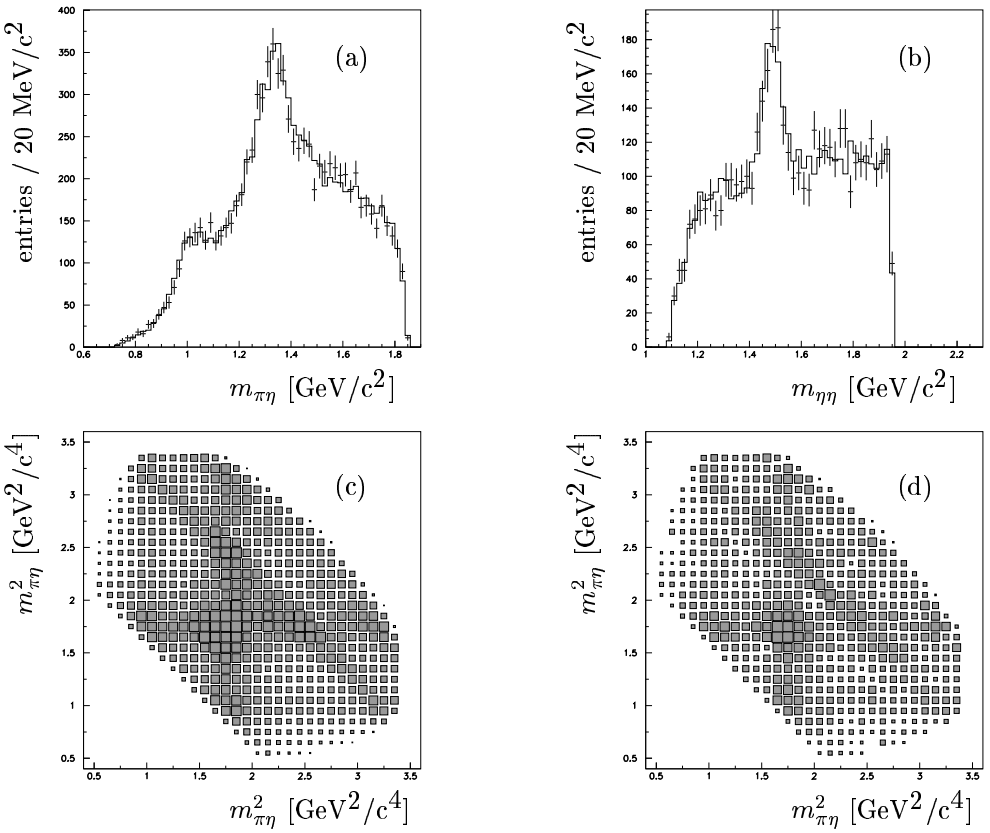

Figure 3.2: **Dalitz plot and invariant mass spectra of the basic fit.** *In spectra (a) and (b) the projections in $\pi\eta$ and $\eta\eta$ are shown. The solid line shows the fit, the error bars the data. Below the Dalitz plots of the fit (c) and the data (d) are presented. The resolution is 0.1 GeV^2/c^4 per bin.*

3.2 Basic fit including other resonances

To test the presence of other resonances in the data a $f_J(1700)$, $\hat{\rho}(1400)$, $f_2(1525)$ and $a_2(1680)$ are introduced in turn. Note that only the change in NLL can be compared, not the absolut value.
We also tried an $a_0(1450)$. It was refused by the fit.

3.2.1 Basic fit + $f_J(1700)$

To the basic fit a $f_J(1700)$ at 1750 MeV/c^2 with a width of 250 MeV/c^2 was added. Also interferences with $a_0(980)$ and $a_2(1320)$ were taken into account.
Spin 0 was rejected by the fit completely. A fit with spin 2 and 31 parameters resulted in a NLL of -451, which is a change of 26 compared to the basic fit with 23 parameters. Fig. 3.3 visualize the fit results. To check the chosen mass and width for this resonance a scan of these parameters was performed. The result is shown in fig 3.4. There is no significant change in NLL over the complete scan range.

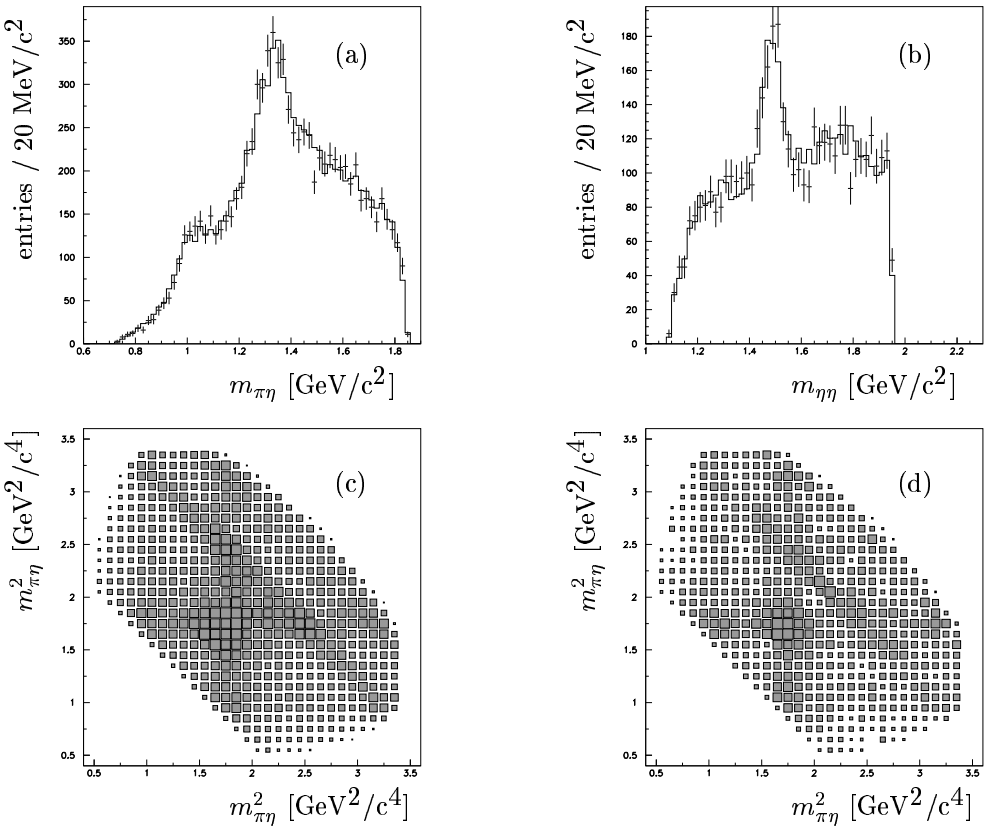

Figure 3.3: **Dalitz plot and invariant mass spectra of the basic fit including a $f_2(1700)$.** *In spectra (a) and (b) the projections in $\pi\eta$ and $\eta\eta$ are shown. The solid line shows the fit, the error bars the data. Below the Dalitz plots of the fit (c) and the data (d) are presented. The bin size is 0.1 GeV^2/c^4.*

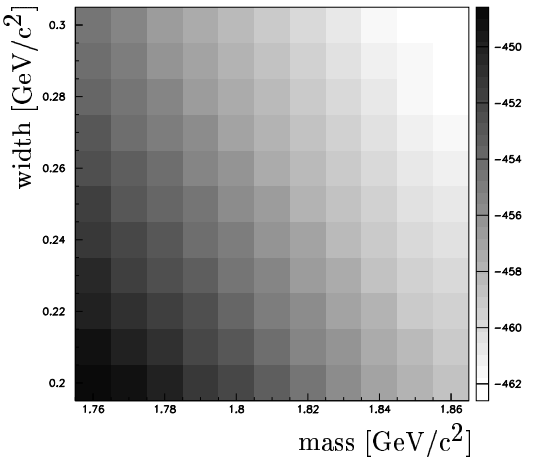

Figure 3.4: **Mass/width scan of a $f_2(1700)$.** *The scan shows no significant change in NLL over the complete range. At higher masses and widths the edge of the reduced Dalitz plot is reached. The major part of the resonance is outside the data region.*

3.2.2 Basic fit + $f_2(1525)$

A $f_2(1525)$ was added to the basic fit including interferences with $a_0(980)$ and $a_2(1320)$. For mass and width PDG values were chosen: (1525 ± 76) MeV/c^2. The fit ended up with a NLL of -434 using 31 parameters. This is only a change of 9 in NLL compared to the basic fit. This change is not significant enough compared to the increase of fitted parameters by 9. Therefore a $f_2(1525)$ can be excluded from the data. Again a mass/width scan was done but also no minimum in NLL could be found. Figures 3.5 and 3.6 display the fit results.

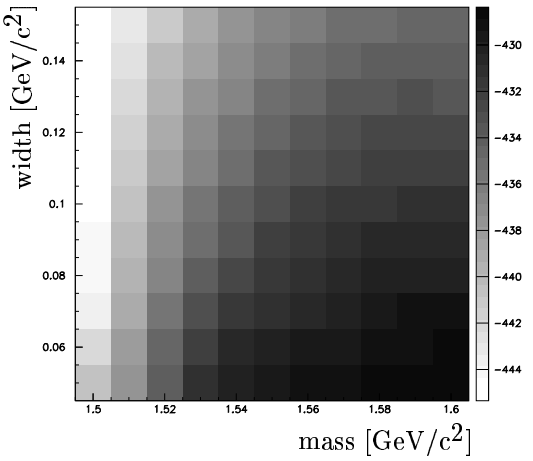

Figure 3.5: **Mass/width scan of a $f_2(1525)$.** *The scan shows no significant change in NLL over the complete range. At lower masses the region of the $f_0(1500)$ is described by the additional $f_2(1525)$.*

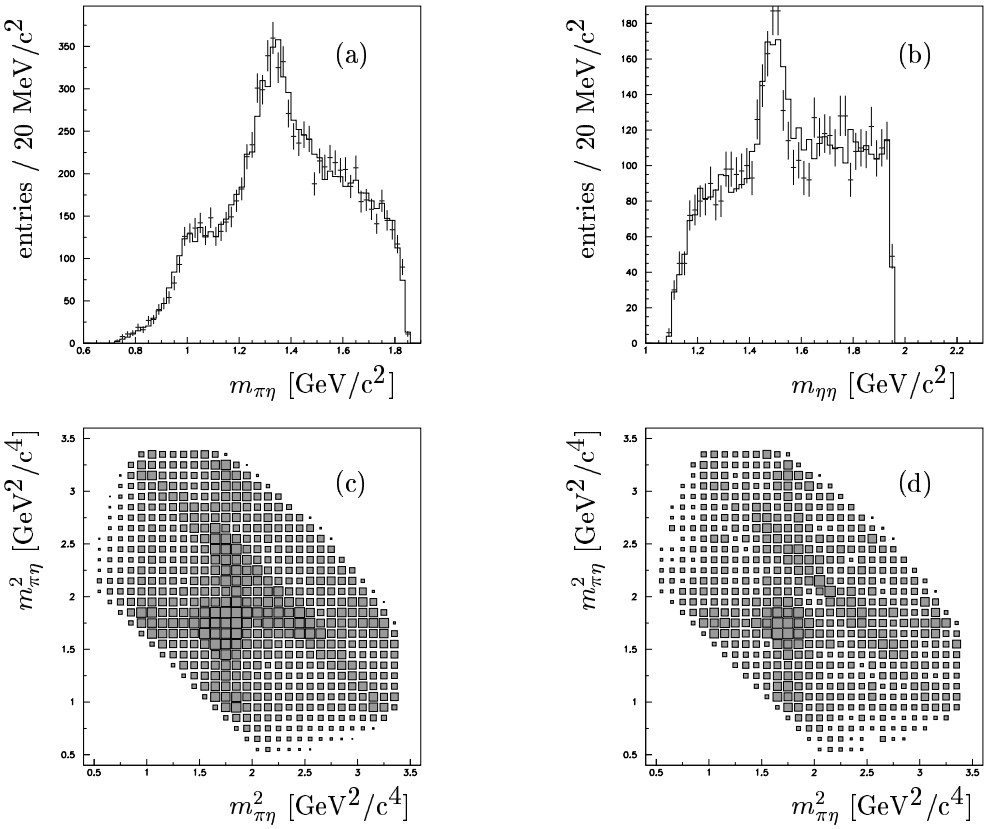

Figure 3.6: **Dalitz plot and invariant mass spectra of the basic fit including a $f_2(1525)$.** *In spectra (a) and (b) the projections in $\pi\eta$ and $\eta\eta$ are shown. The solid line shows the fit, the error bars the data. Below the Dalitz plots of the fit (c) and the data (d) are presented. The bin size is 0.1 GeV^2/c^4.*

3.2.3 Basic fit + $\hat{\rho}(1400)$

We included a $\hat{\rho}(1400)$ with mass = 1430 MeV and width = 300 MeV into the basic fit and added also the following interferences: $\hat{\rho}(1400)$ x $a_2(1320)$, $\hat{\rho}(1400)$ x $f_0(1500)$, $\hat{\rho}(1400)$ x itself. In addition mass and width of the $a_2(1320)$ were slightly changed to (1320 $\pm$ 170) MeV/c^2. We proceeded similarly for $f_0(1500)$: (1490 $\pm$ 50) MeV/c^2. The fit gives a NLL of -445 using 31 parameters, which is by 20 lower than the basic fit. Here we performed a mass/width scan, too. The spectra of the fit and the scan are shown in figures 3.7 and 3.8.

The conclusion of these extensions of the basic fit is, that none of these states under study gave a convincing reduction of NLL, taking into account the increased number of free parameters.

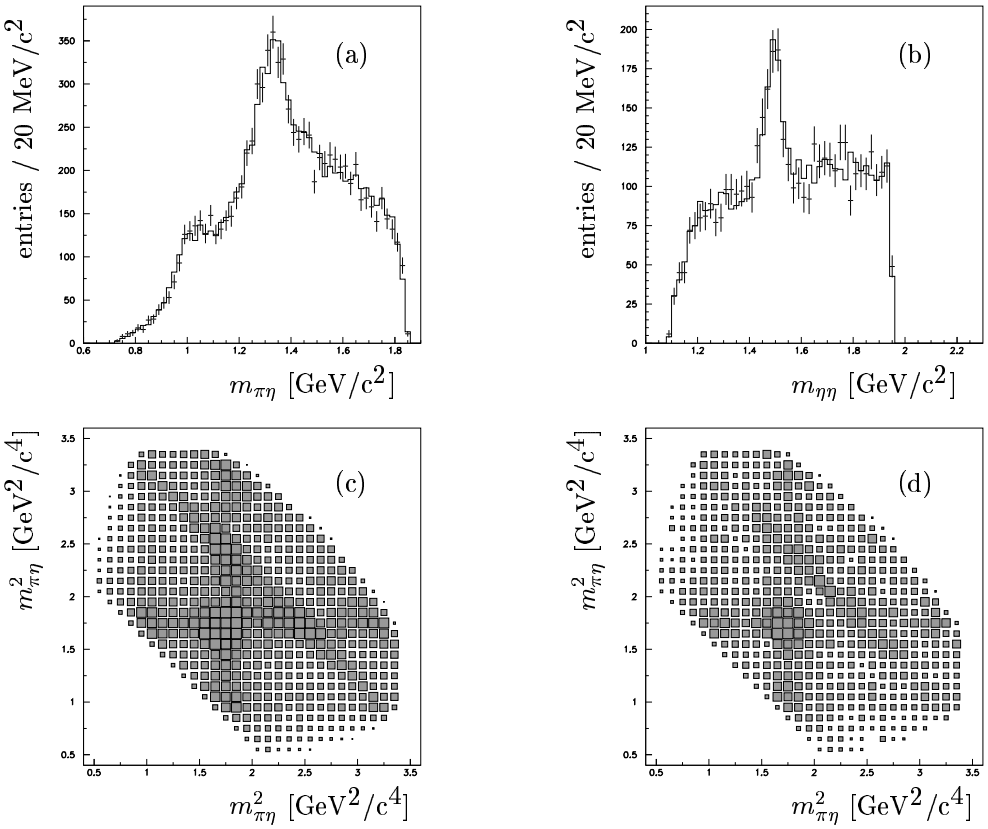

Figure 3.7: **Dalitz plot and invariant mass spectra of the basic fit including a $\hat{\rho}$(1400).** *In spectra (a) and (b) the projections in $\pi\eta$ and $\eta\eta$ are shown. The solid line shows the fit, the error bars the data. Below the Dalitz plots of the fit (c) and the data (d) are presented. The resolution is 0.1 GeV^2/c^4 per bin.*

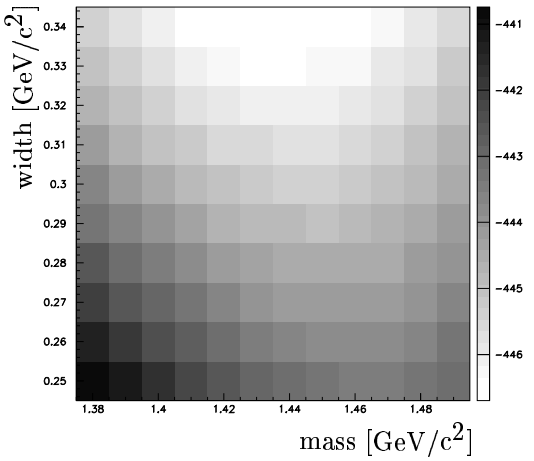

Figure 3.8: **Mass/width scan of a $\hat{\rho}$(1400).** *Only very high widths above 320 MeV lead to an improvement for the fit. In this case the resonance covers the whole phase space of the reduced Dalitz plot.*

3.2.4 Basic fit + $a_2(1680)$

After having no success with introducing known but not well established resonances we tried a new isovector state with spin 2, mass = 1635 MeV/c^2 and width = 300 MeV/c^2. Adding interferences with $a_0(980)$ and $a_2(1320)$ and changing the width of $a_2(1320)$ to 130 MeV/c^2 we ended up with a NLL of -494 and 31 parameters. This is a significant improvement of the fit by 69 compared to the basic fit. The spectra of the fitresults are presented in fig. 3.9. As one can see not only the region around $m_{\pi\eta}$ =1650 MeV/c^2 is described very well but the region around $m_{\pi\eta}$ = 1400 MeV/c^2 is also fitted in a proper way. To check wether the found state is a genuine resonance or not a mass/width scan was performed (fig. 3.10). The scan shows a clear minimum which is typical for a resonance. This behaviour is missing for the other tested resonances.

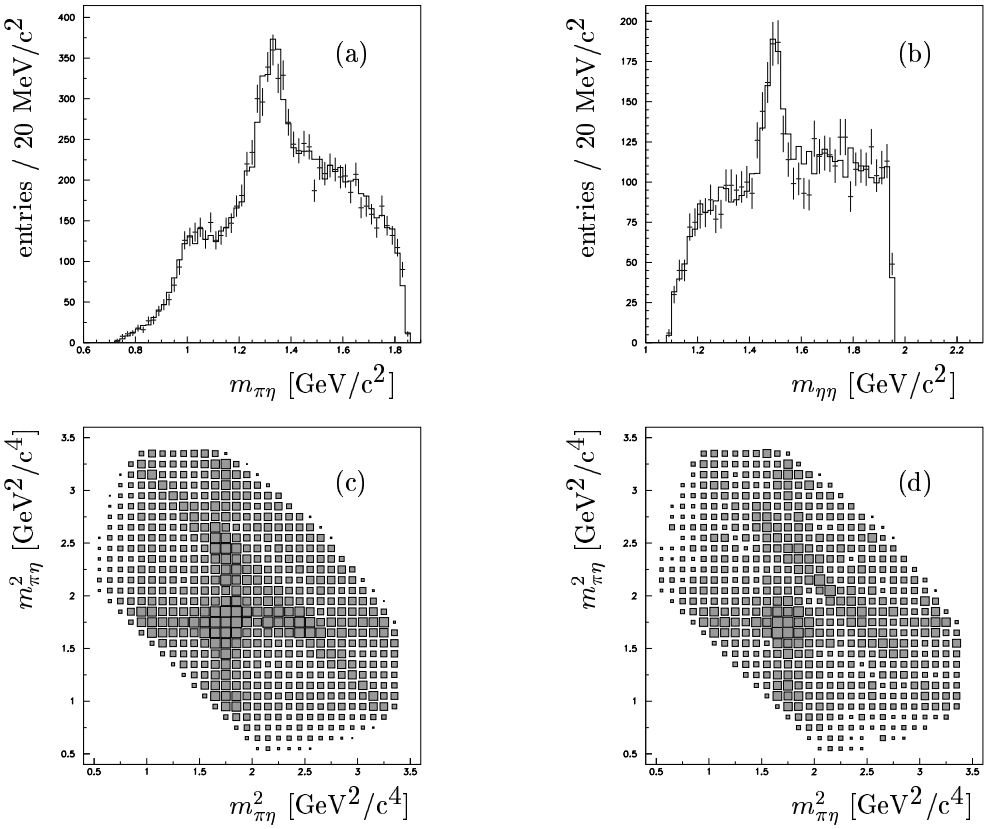

Figure 3.9: **Dalitz plot and invariant mass spectra of the basic fit including a $a_2(1680)$.** *In spectra (a) and (b) the projections in $\pi\eta$ and $\eta\eta$ are shown. The solid line shows the fit, the error bars the data. Below the Dalitz plots of the fit (c) and the data (d) are presented. The resolution is 0.1 GeV^2/c^4 per bin.*

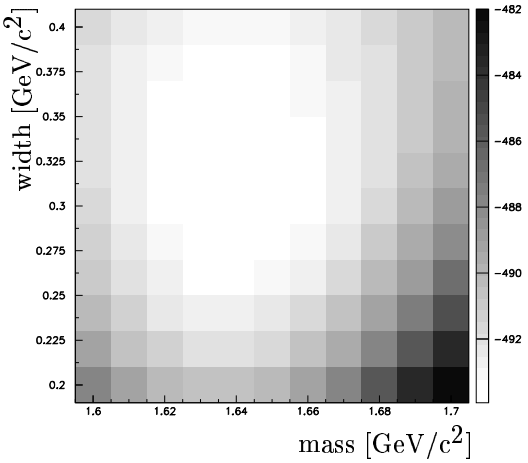

Figure 3.10: **Mass/width scan of a $a_2(1680)$.** *A clear minimum can be observed at 1635/300 MeV/c^2 which is typical for a resonance.*

3.3 Extended fit on full Dalitz plot

After the successful description of the reduced Dalitz plot using five resonances ($a_0(980)$, $a_2(1320)$, $a_2(1680)$, $f_2(1270)$, $f_0(1500)$) and various interferences we fitted the full Dalitz plot with the same ingredients. Using the same parameters (magnitudes, phases, coherence factors) the fit resulted in a NLL of -338 (fig. 3.11). After optimization of magnitudes, phases and coherence factors the fit ended up with a NLL of -452 with 31 parameters (fig. 3.12). Still there are discrepancies between fit and data. Obviously there is a problem at the $a_0(980)$ crossing region which corresponds to the $\eta\eta$-mass region above 2 GeV/c^2. This region can't be explaind by $a_0(980)$ crossing alone and suggests the presence of an $\eta\eta$ resonance around 2.2 GeV/c^2.

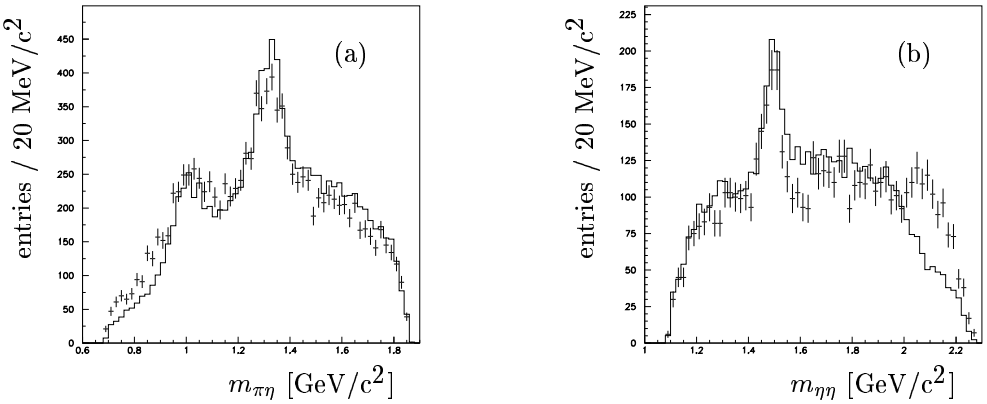

Figure 3.11: **Invariant mass spectra of the extended fit before optimization.** *In spectra (a) and (b) the projections in $\pi\eta$ and $\eta\eta$ are shown. The solid line shows the fit, the error bars the data.*

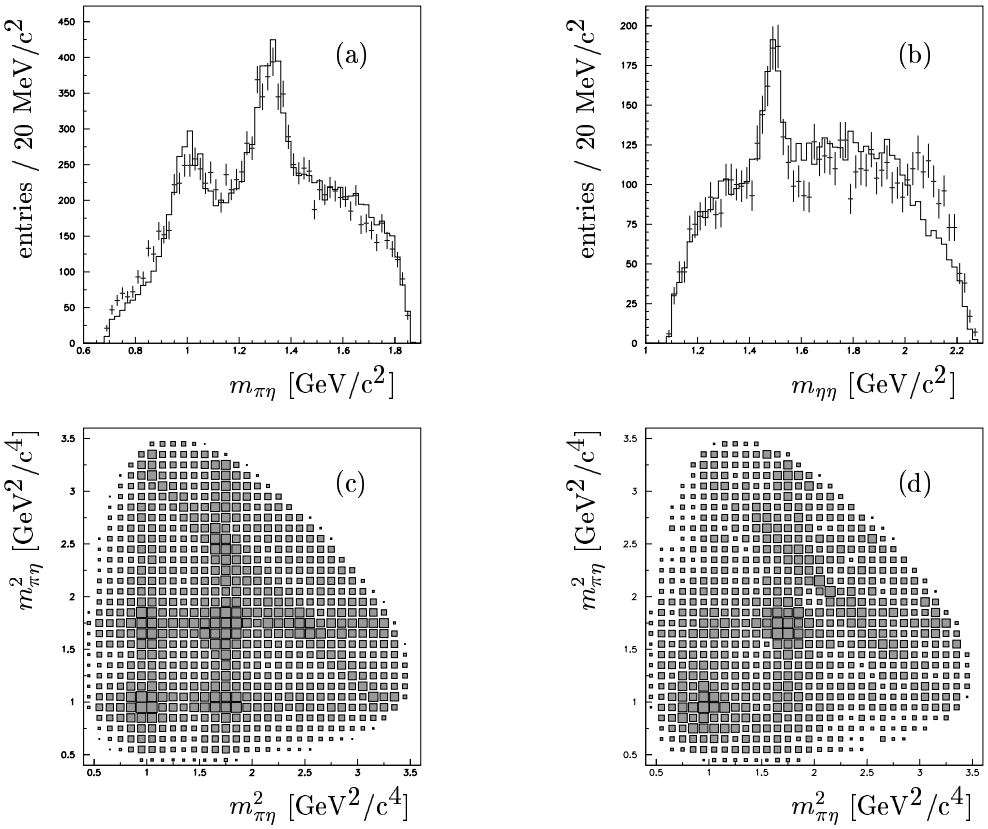

Figure 3.12: **Dalitz plot and invariant mass spectra of the extended fit after optimization.** *In spectra (a) and (b) the projections in $\pi\eta$ and $\eta\eta$ are shown. The solid line shows the fit, the error bars the data. Below the Dalitz plots of the fit (c) and the data (d) are presented. The bin size is 0.1 GeV^2/c^4.*

3.4 Extended fit including a $f_J(2100)$

To describe the $\eta\eta$-region around 2.2 GeV/c^2 we introduced a $f_J(2100)$-state at 2130 MeV/c^2 with Γ=250 MeV/c^2 and added interferences with $a_0(980)$ and $a_2(1320)$. Testing spin 0, 2 and 4 the fit ended up with the NLLs given in table 3.3. Figure 3.13 shows the spectra of these fits.

Spin	NLL	ΔNLL	Δ# parameter
0	-575	123	4
2	-637	185	8
4	-668	216	10

Table 3.3: **Fit results using a $f_J(2100)$ with various spins.** *The value for ΔNLL was calculated in comparison to the NLL of the extended fit without an $f_J(2100)$-state.*

From these fits one can state that spin 0 is unlikely (NLL is worse by 62 compared to spin 2). Spin 2 is prefered by the fit, but spin 4 can't be excluded.

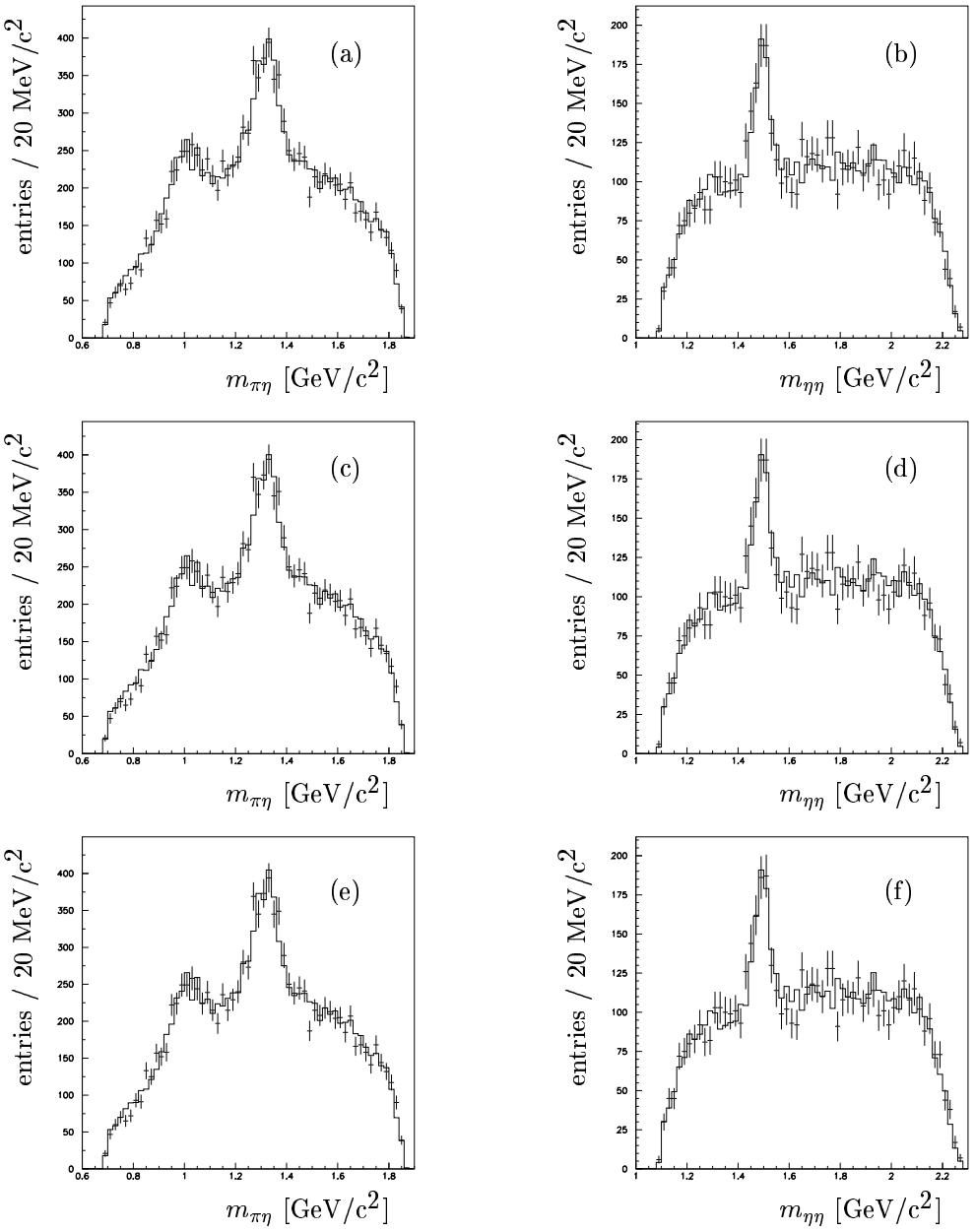

Figure 3.13: **Invariant mass spectra of the extended fit including a $f_J(2100)$.** *In spectra (a) and (b) the projections in $\pi\eta$ and $\eta\eta$ for spin 0 are shown. Spectra (c) and (d) present a fit with spin 2 and spectra (e) and (f) a fit with spin 4.*

3.5 Mass and widths scans

To check if all resonances are at their 'right' mass/width values independent mass/width scans were performed. That means scanning the mass and width of one resonance while fixing the remaining ones. The scans were done using a fixed $f_J(2100)$ at 2130/250 MeV/c^2 with spin 2. Table 3.4 gives the ranges and the values for the best NLL of the scans and

figure 3.14 gives the details of these scans.

Resonance	mass range [MeV/c^2]	width range [MeV/c^2]	best values of mass/width [MeV/c^2]
$a_0(980)$	970 - 1015	100 - 170	990/140
$a_2(1320)$	1300 - 1340	100 - 220	1320/150
$a_2(1650)$	1620 - 1770	200 - 400	1680/270
$f_2(1270)$	1230 - 1350	140 - 360	1320/150
$f_0(1500)$	1470 - 1515	40 - 110	1490/ 50

Table 3.4: **Ranges and best values of the mass/width scans.** *The scans were done independently with the other resonances held fix.*

Using the best mass/width values from tab. 3.4 also a mass/width scan of $f_J(2100)$ was performed with spin 0, 2 and 4. The results are shown in fig. 3.15. One finds that for spin 2 the width tends to be large. This influences the low mass region. The scan of spin 4 was unstable due to too many parameters, i. e. its results depended very critically on the initial parameter set. Best values are given in the table below.

Spin	best values of mass/width [MeV/c^2]
0	2140/230
2	2130/290
4	2170/280

Table 3.5: **Best values of the $f_J(2100)$ mass/width scans.** *Note that the scan of spin 4 was unstable, i. e. the best value depends strongly on the initial fitting parameter set (see fig. 3.15).*

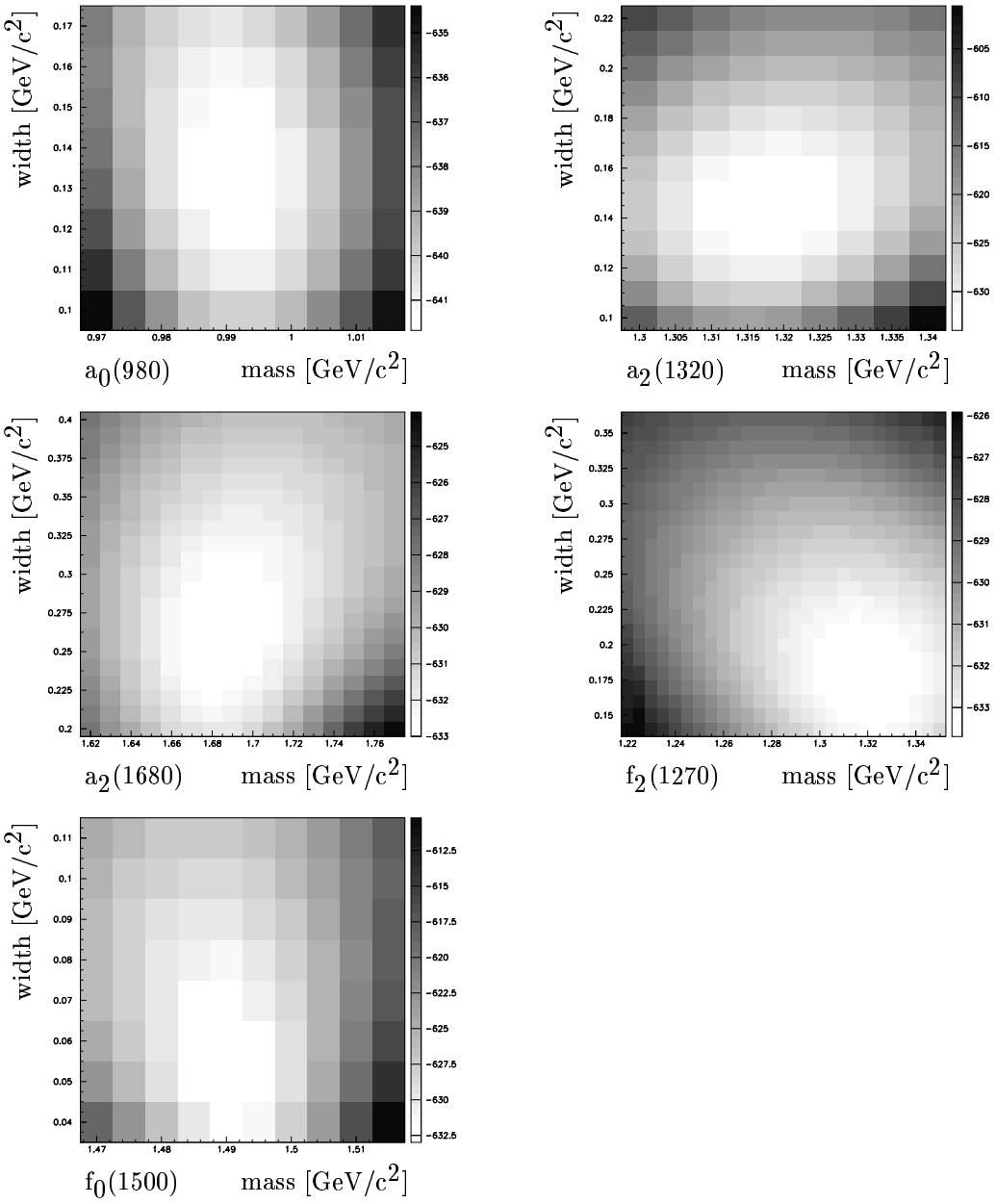

Figure 3.14: **Mass/width scan of the fitted resonances.** *Every scan shows a clear and sharp minimum which demonstrates the necessity of taking into account this resonance.*

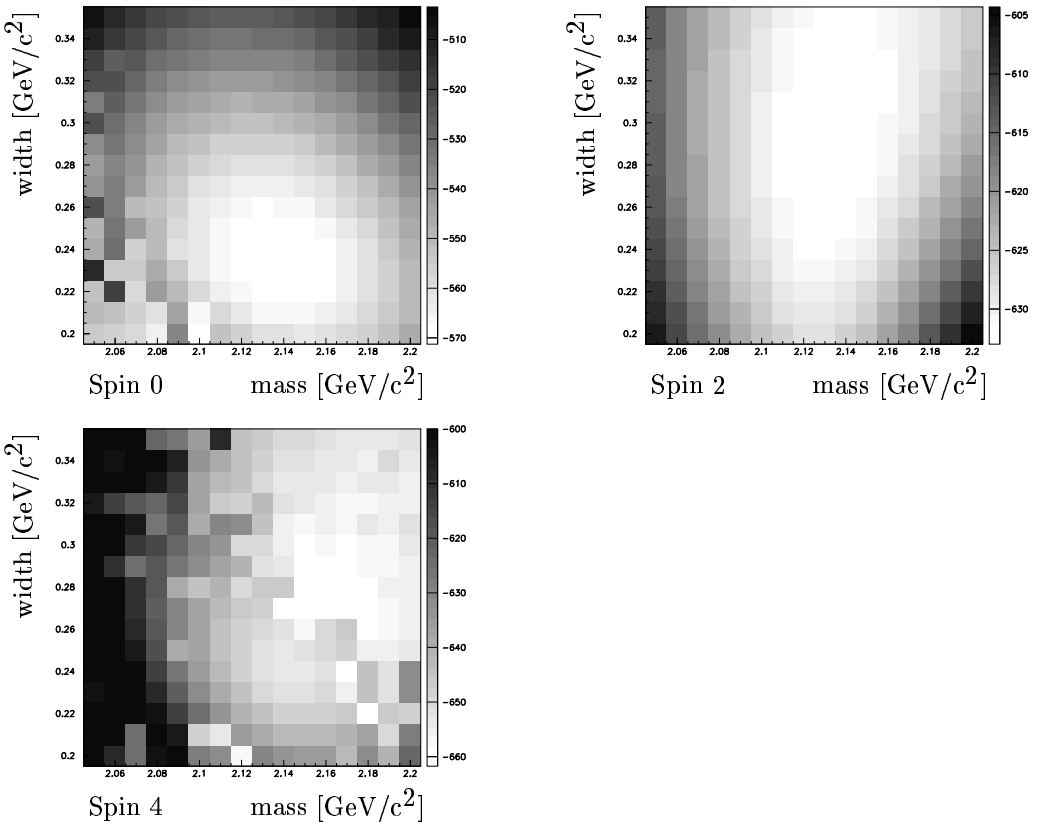

Figure 3.15: **Mass/width scan of $f_J(2100)$ for spin 0, 2 and 4.** *Note that the scan for spin 4 was unstable and the best value for the mass/width is uncertain.*

3.6 Best Fit after mass/width scans

Using the best values for masses and widths determined by the scans the best fit to the data ended up with an NLL of -648 and 39 parameters. The spectra are shown in figure 3.16 and the used masses and widths are summarized in table 3.6. In this table also the contribution of the resonances to the fit are given. The contribution is calculated without considering the interferences. To visualize the goodness of the fit in figure 3.17 the difference of χ^2 is plotted for the cases where the fit is greater than the data and vice versa. The spectra are normalized to 3 $\sigma = 9$. The errors are discussed in Chapter 4.

Resonance	mass/width [MeV/c^2]	contribution [%]
$a_0(980)$	990/140	12
$a_2(1320)$	1320/150	41
$a_2(1680)$	1680/270	16
$f_2(1270)$	1320/150	5
$f_0(1500)$	1490/ 50	5
$f_2(2100)$	2130/290	18
background (chapter 3.10)		3

Table 3.6: **Mass/width values used for the best fit.** *The contributions of each resonance are calculated without consideration of the interferences.*

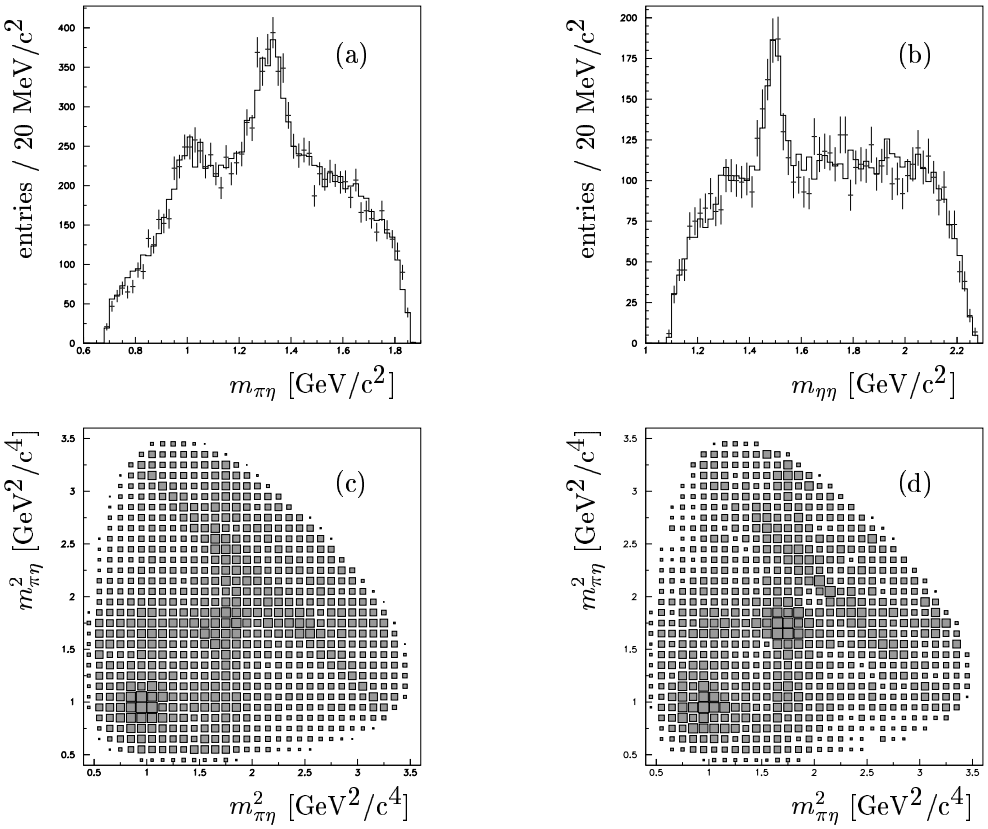

Figure 3.16: **Dalitz plot and invariant mass spectra of the best fit.** *In spectra (a) and (b) the projections in $\pi\eta$ and $\eta\eta$ are shown. The solid line shows the fit, the error bars the data. Below the Dalitz plots of the fit (c) and the data (d) are presented. The bin size is 0.1 GeV^2/c^4.*

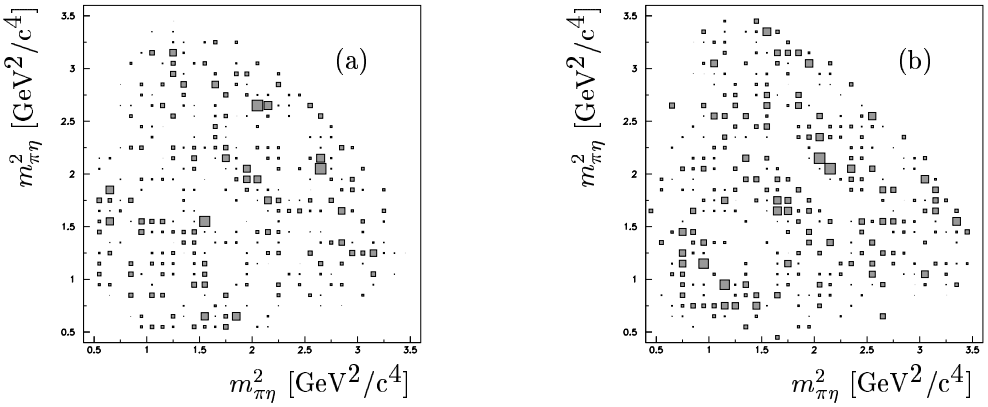

Figure 3.17: **χ^2 distribution of the best fit.** *In spectrum (a) $\Delta\chi^2$ is plotted for the case fit > data and in spectrum (b) the case fit < data is shown. The spectra are normalized to 3 σ = 9.*

3.7 Test of other high mass $\eta\eta$-resonances

Looking at figure 3.16 (b) the description of the $\eta\eta$-mass region from 1600 to 2000 MeV/c^2 seems not to be perfect. Therefore a further $\eta\eta$ resonance in the mass range between 1600 and 2000 MeV/c^2 was introduced. Unfortunatelly the fit was too unstable. Some mass/width scans determined a 'sharp' minimum but starting at this evaluated mass/width value no improvement was found in further scans. From these tests the existence of a $\eta\eta$-resonance between 1.7 and 1.9 GeV/c^2 can't be excluded. But for a good description of these data such a state is not needed.

3.8 Fit of the high mass $\eta\eta$-region

To perform a crosscheck on the existence of the $f_2(2100)$ we applied a cut on $m^2(\eta\eta) < 3.8$ GeV^2/c^4 and fitted the remaining Dalitz plot (1.338 data and 4.543 Monte Carlo events, fig. 3.18) using only the $a_0(980)$, the $a_2(1320)$, the $f_2(2100)$ and the interferences between them.

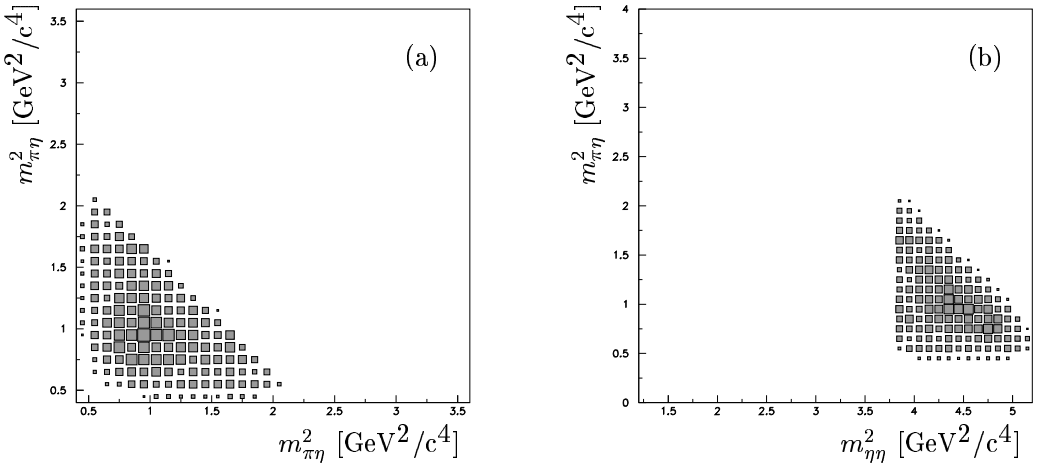

Figure 3.18: **Reduced Dalitz plot $\pi^0\eta\eta$ for crosscheck.** *The symmetric (a) and asymmetric (b) Dalitz plots are shown. The bin size is 0.1 GeV^2/c^4.*

3.8.1 Basic fit without $f_2(2100)$

In the basic fit we fitted the $a_0(980)$ at 990/140 MeV/c^2 and the $a_2(1320)$ at 1320/130 MeV/c^2. In addition we took the interferences $a_0(980)$ x $a_2(1320)$ and $a_0(980)$ x $a_0(980)$ into account. The $a_2(1320)$ crossing region is outside the considered part of the Dalitz plot. Therefore no $a_2(1320)$ self interference is fitted. The fit resulted in a NLL of -22 using 6 parameters. The spectra are shown in fig. 3.19. Clearly a discrepancy in the $\eta\eta$ mass projection is visible.

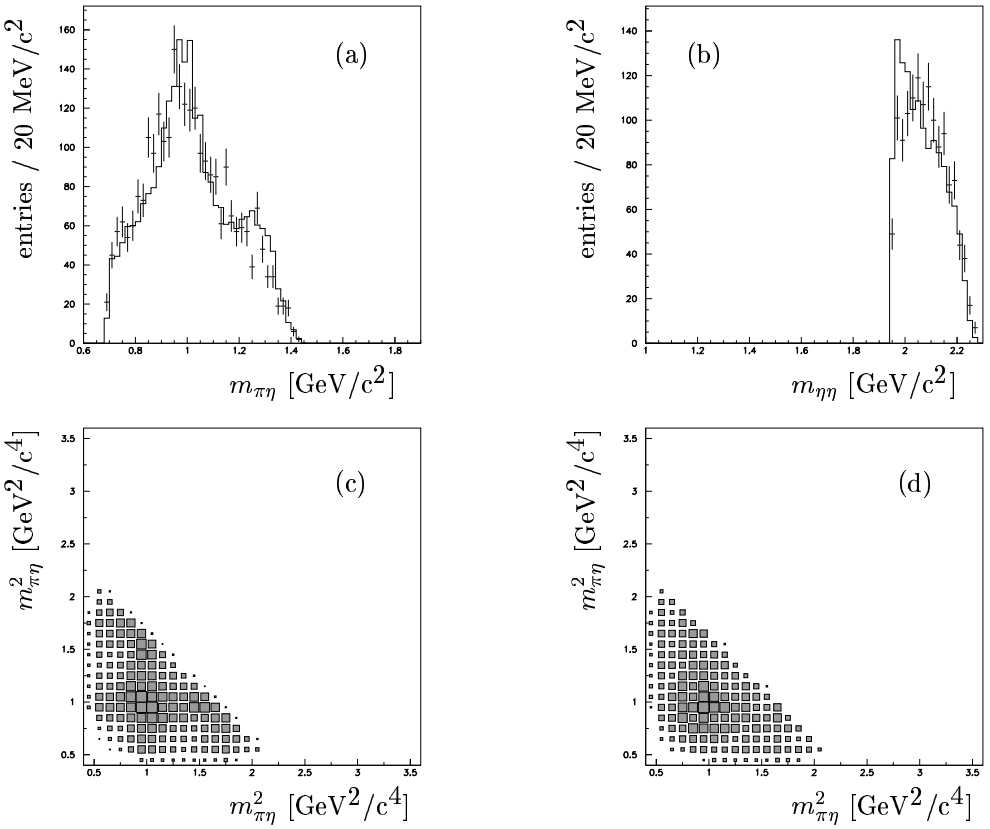

Figure 3.19: **Dalitz plot and invariant mass spectra of the basic high mass region fit.** *In spectra (a) and (b) the projections in $\pi\eta$ and $\eta\eta$ are shown. The solid line shows the fit, the error bars the data. Below the Dalitz plots of the fit (c) and the data (d) are presented. The bin size is 0.1 GeV^2/c^4.*

3.8.2 Basic fit + $f_2(2100)$

To the basic fit we added the $f_2(2100)$ at 2130/290 MeV/c^2 and its interferences with $a_0(980)$ and $a_2(1320)$. The NLL for this fit decreased to -108 using 14 parameters which gives a difference of 86 compared to the basic fit using 8 parameters. In figure 3.20 the results of the extended fit are shown. Like the value of NLL the projections and Dalitz plots demonstrate the necessity of a $f_J(2100)$ in this region.

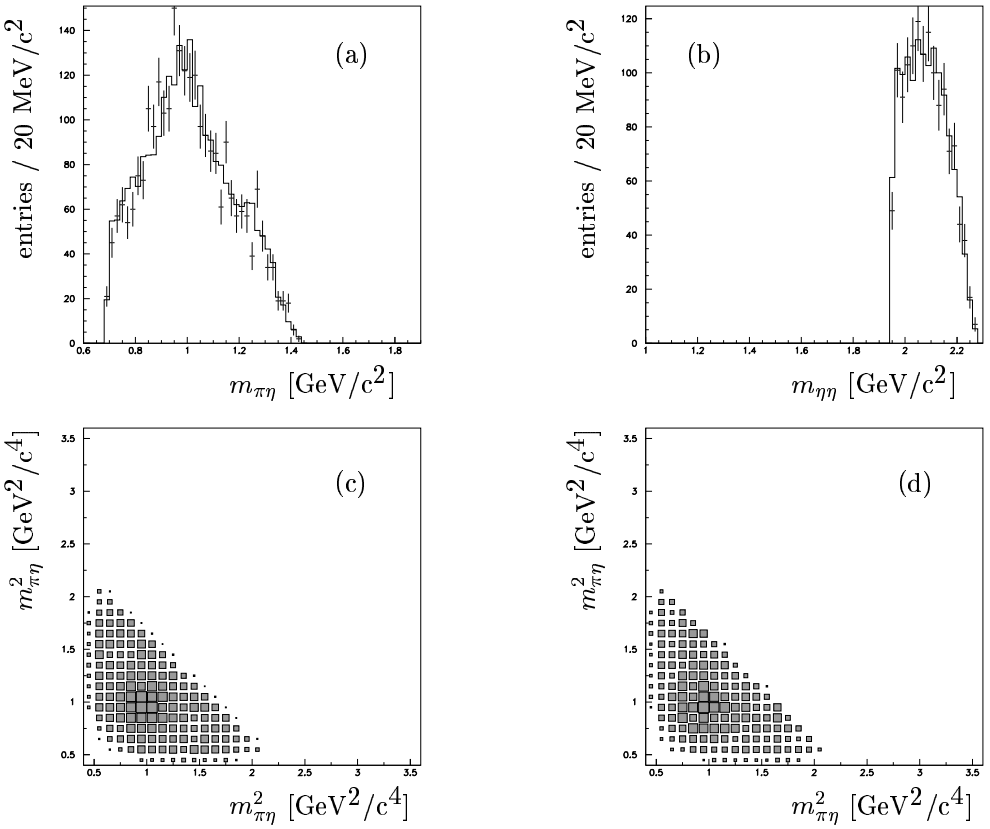

Figure 3.20: **Dalitz plot and invariant mass spectra of the extended high mass region fit.** *In spectra (a) and (b) the projections in $\pi\eta$ and $\eta\eta$ are shown. The solid line shows the fit, the error bars the data. Below the Dalitz plots of the fit (c) and the data (d) are presented. The bin size is 0.1 GeV^2/c^4.*

3.9 Comparison to PDG values

The values for masses and widths found by the fit differ considerably from the PDG values for some resonances. To investigate the dependence on the fitted values we inserted the PDG masses and widths in the fit for the four well known resonances $a_0(980)$, $a_2(1320)$, $f_2(1270)$ and $f_0(1500)$. The NLL got worse by 25. Table 3.7 gives the detailed information.

Resonance		Fit [MeV/c^2]	PDG [MeV/c^2]	ΔNLL
$a_0(980)$	M:	990	984	
	Γ:	140	100	-5
$a_2(1320)$	M:	1320	1320	
	Γ:	150	120	-8
$f_2(1270)$	M:	1320	1275	
	Γ:	150	190	-5
$f_0(1500)$	M:	1490	1500	
	Γ:	50	100	-7
				-25

Table 3.7: **Comparison with PDG values.** *Each resonance is varied separately.*

3.10 Background

Some background events at the $\eta\eta$ threshold (at 1095 MeV/c^2) originating from $3\pi^0$ are described by an incoherent Breit-Wigner form at 1100 MeV/c^2 with a width of 150 MeV/c^2. Figure 3.21 shows a mass/width scan of this region. The contribution of this background is 3%

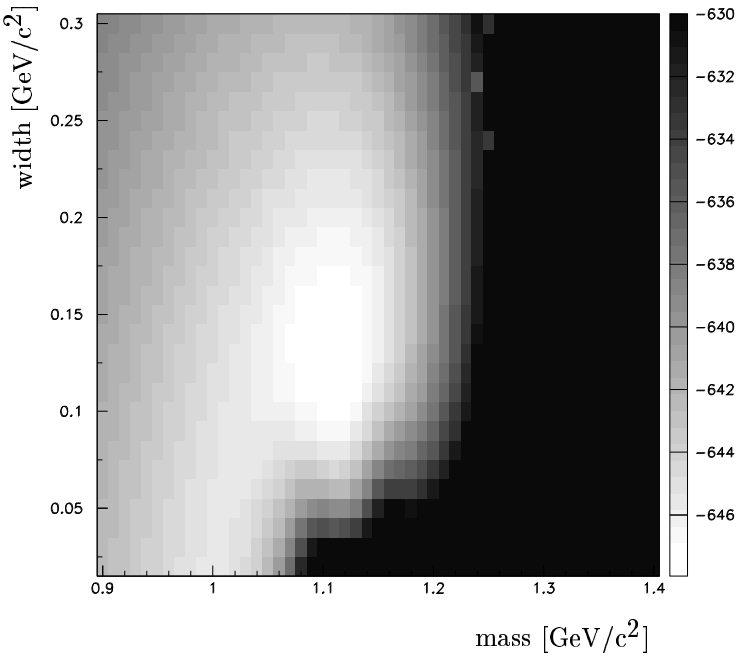

Figure 3.21: **Mass/width scan of $\eta\eta$ threshold region.** *The fit found the lowest NLL at 1120/150 MeV/c^2.*

Chapter 4

Summary

4.1 Fit history

We started to fit a mass reduced Dalitz plot ($m_{\eta\eta}{}^2 < 3.8$ GeV$^2/c^4$) with the basic resonances $a_0(980)$, $a_2(1320)$, $f_2(1270)$ and $f_0(1500)$ and interferences between them. Then we introduced in turn other resonances, from which only a new isovector state $a_2(1680)$ reached a significant change in NLL. Using these five resonances a fit of the full Dalitz plot demonstrates the need of a high $\eta\eta$ mass state around 2.2 GeV/c^2. Fitting a $f_J(2100)$ gave indeed a significant change in NLL. Unfortunatelly the spin couldn't be determined. The fit prefers spin 2 but spin 4 can't be excluded. Spin 0 is unlikely. Tables 4.1 and 4.2 gives a summary of the fit history and the results.

Fit	ΔNLL	# parameters
Basic fit	+69	23
$+a_0(1450)$	+69	23
$+f_0(1700)$	+69	27
$+f_2(1700)$	+43	31
$+\hat{\rho}(1400)$	+49	31
$+f_2(1525)$	+60	31
$+a_2(1680)$	0	31
(extended)		

Table 4.1: **Fit history of the low $\eta\eta$ mass reduced Dalitz plot.** *The value for NLL is compared to the basic fit including the $a_2(1680)$.*

Fit	ΔNLL	# parameters
Extended fit	0	31
$+f_0(2100)$	-123	35
$+f_2(2100)$	-185	39
$+f_4(2100)$	-216	41

Table 4.2: **Fit history of the full Dalitz plot.** *$\Delta NLL = 0$ corresponds to the extended fit including $a_2(1680)$.*

4.2 Final results with errors

The masses and widths of all resonances included in the final fit are listed in Table 4.3 (Col. 1 and 2). The fit resulted in NLL=-648 using 39 parameters. The errors correspond to the values, which produce a change of one in the NLL-values. Column 3 of Table 4.3 gives the percentage contributions of the states to the total intensity in the Dalitz plot. Note, that only the squares of the amplitudes were taken into account, the interferences were neglected. The error corresponds to changes of the masses and widths of the resonances within their errors, always taking the extreme mass/width-combination.

The mass and width values of Table 4.3 in most cases differ from the PDG-values. This is due to the fact, that no Blatt-Weißkopf penetration factors were used and some amplitudes are weak, which prevents a precise determination of the resonance parameters. E.g., using a Blatt-Weißkopf factor for $f_2(1270)$ changes the best fit mass value from 1320 MeV/c^2 to 1250 MeV/c^2, showing the big band of variation in this small amplitude. In order to investigate the dependence of the general conclusions of this paper on the mass/width-values chosen the PDG-values for the already known resonances were used, instead of the masses/widths of Table 4.3. The NLL worsens by 25 and leaves all conclusions regarding the newly found resonances unchanged within the errors given.

Resonance	mass (error) [MeV/c^2]	width (error) [MeV/c^2]	contribution (error) [%]
$a_0(980)$	990 (15)	140 (40)	12 (1)
$a_2(1320)$	1320 (20)	150 (30)	41 (2)
$a_2(1680)$	1680 (40)	270 (70)	16 (1)
$f_2(1270)$	1320 (40)	150 (50)	5 (2)
$f_0(1500)$	1490 (10)	50 (20)	5 (1)
$f_J(2100)$	2130 (30)	290 (50)	18 (1)

Table 4.3: **Masses and widths from the final fit including errors.**

The findings of this analysis are backed up by the analysis of the same annihilation channel in the 10γ-mode, i.e. one η decaying to $3\pi^0$, the remaining η and the π^0 decaying to two γ's [7]. The Dalitz plot and the $\pi^0\eta$- and $\eta\eta$-mass projections found there are given in Fig. 4.1. The fit superimposed uses the same amplitudes as found in this paper apart from a different overall normalization constant. The results of the present analysis are completely confirmed. Fig. 4.2 shows χ^2-values similar to Fig. 3.17, again showing no systematic effects.

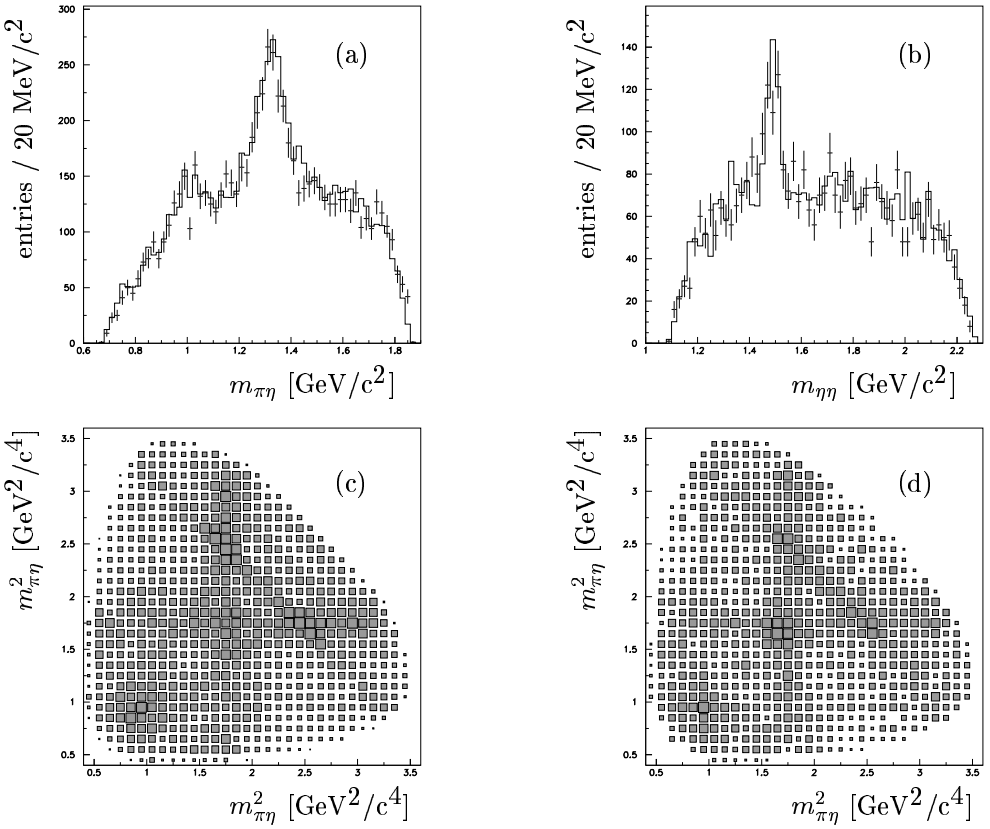

Figure 4.1: **Dalitz plot and invariant massprojections of the $2\eta\pi^0$-channel in its 10γ decay mode from [7].** *(a) $\pi^0\eta$-mass projection and (b) $\eta\eta$-mass projection. The data are plotted as error bars, the fit (identical to the one of the 6γ-mode) is given as full line. (c) fitted Dalitz plot and (d) Data Dalitz plot.*

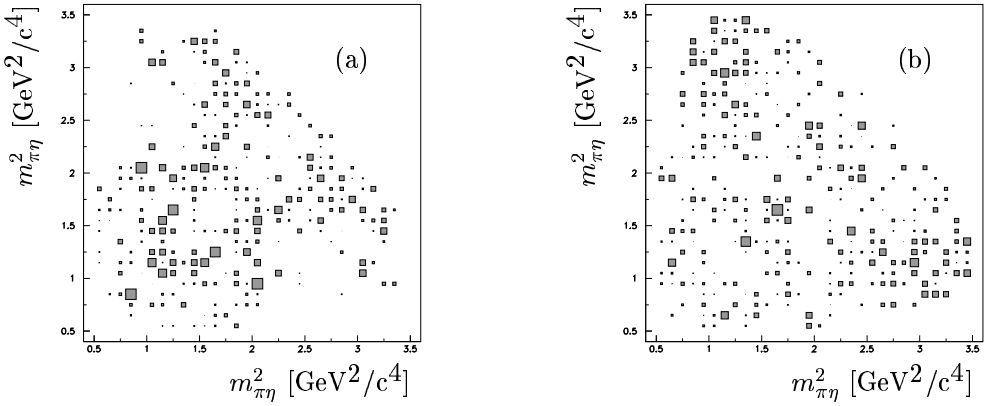

Figure 4.2: **$\Delta\chi^2$ distributions for the fit of the $\pi^0\eta\eta$-10γ-reaction.** *(a) Fit > Data and (b) Fit < Data.*

List of Figures

List of Tables

Bibliography

[1] C.Amsler, *Vertex from neutral events,* CB-note 15

[2] K.Beuchert, *Untersuchungen zur $\overline{p}p$ Annihilation im Fluge am Crystal-Barrel-Detektor,* Ph.D. thesis, University of Bochum, 1995

[3] D.V.Bugg, *Formulae used to fit $\bar{p}p \to 3\pi^0\eta$ in flight,* CB-note 273

[4] R.Glantz, *Untersuchungen zur Richtungsrekonstruktion für Photonen im Crystal-Barrel-Kalorimeter,* Diplomathesis, University of Hamburg, 1992

[5] K.Königsmann, *Fit to unbinned data,* CB-note 195

[6] P.Schmidt, *PED-Energy Correction Function for inflight data,* CB-note 161a

[7] B.Kopf, *Untersuchung des 10γ-Endzustandes bei der $\overline{p}p$ Annihilation im Fluge,* Diploma thesis, University of Bochum, 1997